Schwann cells induce cancer cell dispersion and invasion

Sylvie Deborde,[1] Tatiana Omelchenko,[2] Anna Lyubchik,[1] Yi Zhou,[1] Shizhi He,[1] William F. McNamara,[1] Natalya Chernichenko,[1] Sei-Young Lee,[1] Fernando Barajas,[1] Chun-Hao Chen,[1] Richard L. Bakst,[3] Efsevia Vakiani,[4] Shuangba He,[1] Alan Hall,[2] and Richard J. Wong[1]

[1]Department of Surgery and [2]Cell Biology Program, Memorial Sloan Kettering Cancer Center, New York, New York, USA. [3]Department of Radiation Oncology, Mount Sinai Hospital, New York, New York, USA. [4]Department of Pathology, Memorial Sloan Kettering Cancer Center, New York, New York, USA.

Nerves enable cancer progression, as cancers have been shown to extend along nerves through the process of perineural invasion, which carries a poor prognosis. Furthermore, the innervation of some cancers promotes growth and metastases. It remains unclear, however, how nerves mechanistically contribute to cancer progression. Here, we demonstrated that Schwann cells promote cancer invasion through direct cancer cell contact. Histological evaluation of murine and human cancer specimens with perineural invasion uncovered a subpopulation of Schwann cells that associates with cancer cells. Coculture of cancer cells with dorsal root ganglion extracts revealed that Schwann cells direct cancer cells to migrate toward nerves and promote invasion in a contact-dependent manner. Upon contact, Schwann cells induced the formation of cancer cell protrusions in their direction and intercalated between the cancer cells, leading to cancer cell dispersion. The formation of these processes was dependent on Schwann cell expression of neural cell adhesion molecule 1 (NCAM1) and ultimately promoted perineural invasion. Moreover, NCAM1-deficient mice showed decreased neural invasion and less paralysis. Such Schwann cell behavior reflects normal Schwann cell programs that are typically activated in nerve repair but are instead exploited by cancer cells to promote perineural invasion and cancer progression.

Introduction

Nerves play an important role in cancer invasion. The innervation of prostate and gastric cancers promotes tumor growth and spread (1, 2), and perineural invasion is an aggressive form of cancer cell invasion along nerves. Perineural invasion is associated with a wide variety of malignancies, including pancreatic (up to 100% of cases), prostate (75%–80%), and head and neck cancers (up to 80%), among others (3). Perineural invasion causes patient morbidity through pain and paralysis. Perineural invasion is also associated with an elevated risk of local recurrence and diminished patient survival rates (3, 4). Understanding how cancer invades nerves is an essential step toward developing treatment strategies. Key questions are how cancer cells interact with nerve cells and how they acquire motile and invasive characteristics from these interactions.

Cells from the tumor microenvironment, such as fibroblasts and macrophages, contribute to cancer cell invasion (5–7). These cells facilitate cancer spread through paracrine signaling (5–7) or direct matrix remodeling (5, 8) and also form heterotypic adhesions with cancer cells (9). In nerves, interactions between neurons and Schwann cells involve paracrine functions, matrix remodeling, and direct contact. Schwann cells promote neuronal survival during development and myelinate nerves (10, 11). Importantly, they also facilitate neuronal guidance during nerve repair following traumatic injury (12–15). During nerve repair, Schwann cells induce axonal extensions at sites of contact (16) and form cellular conduits called the bands of Bungner (15). These processes together guide axonal growth and nerve regeneration.

The variety of functions carried out by Schwann cells is supported by their ability to reversibly dedifferentiate and redifferentiate into subtypes with different phenotypes (17). Following nerve injury, Schwann cells dedifferentiate, lose their ability to myelinate, become more motile, and promote neuronal guidance during repair. This is accompanied by reexpression of proteins lost during the myelinating differentiation program, such as glial fibrillary acidic protein (GFAP) and neural cell adhesion molecule 1 (NCAM1) (18–20). Paracrine signaling has been implicated in perineural invasion, with nerve-secreted factors, including glial cell line–derived neurotrophic factor (GDNF), enhancing cancer cell invasion along nerves (3, 4, 21). Schwann cells have been identified at neoplastic sites prior to the onset of cancer invasion (22). The capabilities that Schwann cells acquire during the process of nerve repair have not been investigated in the context of cancer invasion. We reasoned that the Schwann cell's ability to guide cells, remodel matrix, and secrete paracrine signals might facilitate cancer invasion.

To explore the relationship between cancer cells and Schwann cells, we studied in vivo murine and in vitro coculture models of perineural invasion. Cancer cells associate with GFAP$^+$ Schwann cells (GFAP$^+$ SCs) in patient specimens and a murine model of perineural invasion. Schwann cells promote cancer invasion through direct contact, while paracrine signaling and remodeling

▶ Related Commentary: p. 1242

Conflict of interest: The authors have declared that no conflict of interest exists.
Submitted: July 10, 2015; **Accepted:** January 26, 2016.
Reference information: *J Clin Invest*. 2016;126(4):1538–1554. doi:10.1172/JCI82658.

of the matrix are not sufficient to induce invasion. Schwann cells stimulate cancer cell protrusions at sites of cell-cell contact and promote detachment and dispersion of individual cancer cells from neighboring cancer cells. This activity strongly promotes cancer invasion and is dependent on the expression of NCAM1 by Schwann cells.

Results

GFAP-expressing Schwann cells associate with cancer cells in murine and human perineural invasion specimens. Schwann cells expressing S100, myelin basic protein, and myelin protein zero dedifferentiate after nerve injury into a nonmyelinating and more active subtype of Schwann cell (GFAP$^+$ SC) that facilitates repair by neuron guidance (17, 20, 23). We investigated the presence of GFAP$^+$ SCs in pancreatic histologic sections with and without tumor from 8 patients with pancreatic adenocarcinoma. As expected, the sections with tumor showed perineural invasion (Figure 1A). Immunofluorescence staining for GFAP and S100 revealed a significantly higher number of nerves expressing GFAP in the tumor sections as compared with that in the matched control sections (Figure 1, A–C), with an average 3-fold increase in the percentage of GFAP$^+$ SCs per slide (Figure 1C). Nerves were graded as having no GFAP expression, moderate expression, or high GFAP expression (see Supplemental Figure 1A; supplemental material available online with this article; doi:10.1172/JCI82658DS1). We noticed that highly infiltrated nerves showed only moderate staining for both GFAP and S100, an observation likely due to loss of nerve tissue from cancer replacement (Supplemental Figure 1B). We used a murine xenograft model of perineural invasion and assessed for GFAP expression in sciatic nerves injected with either human cancer cells or sterile PBS. Immunofluorescence staining of longitudinal sections of murine sciatic nerve injected with the human pancreatic cancer cell line MiaPaCa-2 or Panc1 showed higher expression of GFAP$^+$ SCs as compared with nerves injected with PBS (Figure 1, D–F). In contrast, the presence of cancer cells reduced the number of myelin$^+$ Schwann cells (Figure 1, G–I). These data suggest that the presence of cancer cells in a nerve leads to an upregulation of GFAP in Schwann cells, similar to the profile of dedifferentiated Schwann cells during nerve repair.

In human specimens with perineural invasion, we detected close associations between GFAP$^+$ SCs and cancer cells in pancreatic adenocarcinoma (Figure 2A), thyroid cancer (Figure 2B), salivary duct carcinoma (Supplemental Figure 2A), and cutaneous squamous cell carcinoma (Supplemental Figure 2B). Figure 2A depicts these associations in adjacent transverse sections of pancreatic adenocarcinoma specimens with perineural invasion stained with H&E for recognition of nerve and cancer cells and stained with anti-GFAP and S100 antibodies for recognition of Schwann cells. The large caliber of cranial nerves allowed for nerve isolation and creation of longitudinal histological sections. Longitudinal sections allow for optimal visualization of Schwann cells in cancer-infiltrated nerves. An infiltrated segment of the recurrent laryngeal nerve from a patient who underwent surgical resection of a poorly differentiated thyroid cancer is depicted in Figure 2, B and C. H&E staining and immunofluorescence using an anti-cytokeratin antibody confirmed nerve infiltration by cancer cells (Figure 2, B and C). GFAP$^+$ SCs closely associated with cancer cells by surrounding a cluster of cancer cells (Figure 2C) or wrapping around individual cells (Supplemental Figure 2C). In contrast, myelin$^+$ Schwann cells were not found in association with cancer cells (Supplemental Figure 2D).

In mice, GFAP$^+$ SCs exhibited long projections that were closely associated with large nucleated cancer cells (Supplemental Figure 2E). After injecting cancer cells that stably express farnesylated red fluorescent plasma membrane protein (F-RFP), we observed associations between GFAP$^+$ SCs and cancer cells (Figure 2D). Collectively, these experiments reveal an increase of GFAP$^+$ SCs in the presence of cancer cells and that these Schwann cells closely associate with cancer cells in vivo for several different cancer types.

Schwann cells recruit cancer cells to nerve projections of DRG explants. To investigate the dynamic interactions between cancer cells and Schwann cells, we cocultured cancer cells with dorsal root ganglion (DRG) explants, using an in vitro model previously described to study perineural invasion (21, 24–27). Freshly extracted DRGs cultured in a drop of Matrigel grow axonal projections (neurites) radially within a week. Immunofluorescence confirmed the presence of both neurites and associated Schwann cells, using Tuj1 and GFAP, respectively, as markers (Supplemental Figure 3). When DRGs were cocultured with MiaPaCa-2 (Figure 3A and Supplemental Video 1) or Panc1 (data not shown) cells expressing the red plasma membrane marker F-RFP, cancer cells were recruited to neurites within 24 to 48 hours and then migrated toward the center of DRGs along neurites, as reported previously (21, 24). Cancer cells not in contact with the DRG either did not move or moved only slowly (Figure 3B).

Immunofluorescence staining using anti-GFAP antibody revealed a close association between DRG Schwann cells and cancer cells (Figure 3C). Time-lapse videos recorded over a period of 24 hours revealed that Schwann cells were highly dynamic, moving with speeds of up to 1.5 μm/min and exhibiting frequent back-and-forth movements, leading to repetitive contacts with cancer cells. Cancer cells moved on and along Schwann cells, following the direction of Schwann cell movement (Figure 3D and Supplemental Video 1B). After contact with a Schwann cell, cancer cells typically developed a protrusion (Figure 3E, arrow) at the site of contact and moved directionally toward the Schwann cell while maintaining contact (Figure 3, E and F, inset 1, and Supplemental Video 1C). In contrast, cancer cells not in contact with Schwann cells did not move toward the DRG (Figure 3, E and F, inset 2, and Supplemental Video 1D). During a 24-hour period, 69% of the cancer cells that contacted dynamic Schwann cells moved; of these, 82% moved toward the Schwann cells (n = 49 sites of contact, 24 DRGs). Cancer migration within the DRG involves interactions with Schwann cells, which act as leading cells.

To confirm and directly assess the importance of Schwann cells in the recruitment of cancer cells to neurites, we first depleted Schwann cells from the DRGs with a single 12-Gy radiation dose. Radiation strongly depleted the number of Schwann cells on neurite segments of similar size, while the DRGs retained viability (Figure 4A). Tuj1 staining was similar in both radiated and nonradiated DRGs (Figure 4A), and a time-lapse video showed that irradiated DRG neurites grow outward (Supplemental Figure 3B), though at a slower rate than nonirradiated DRGs. Depletion of

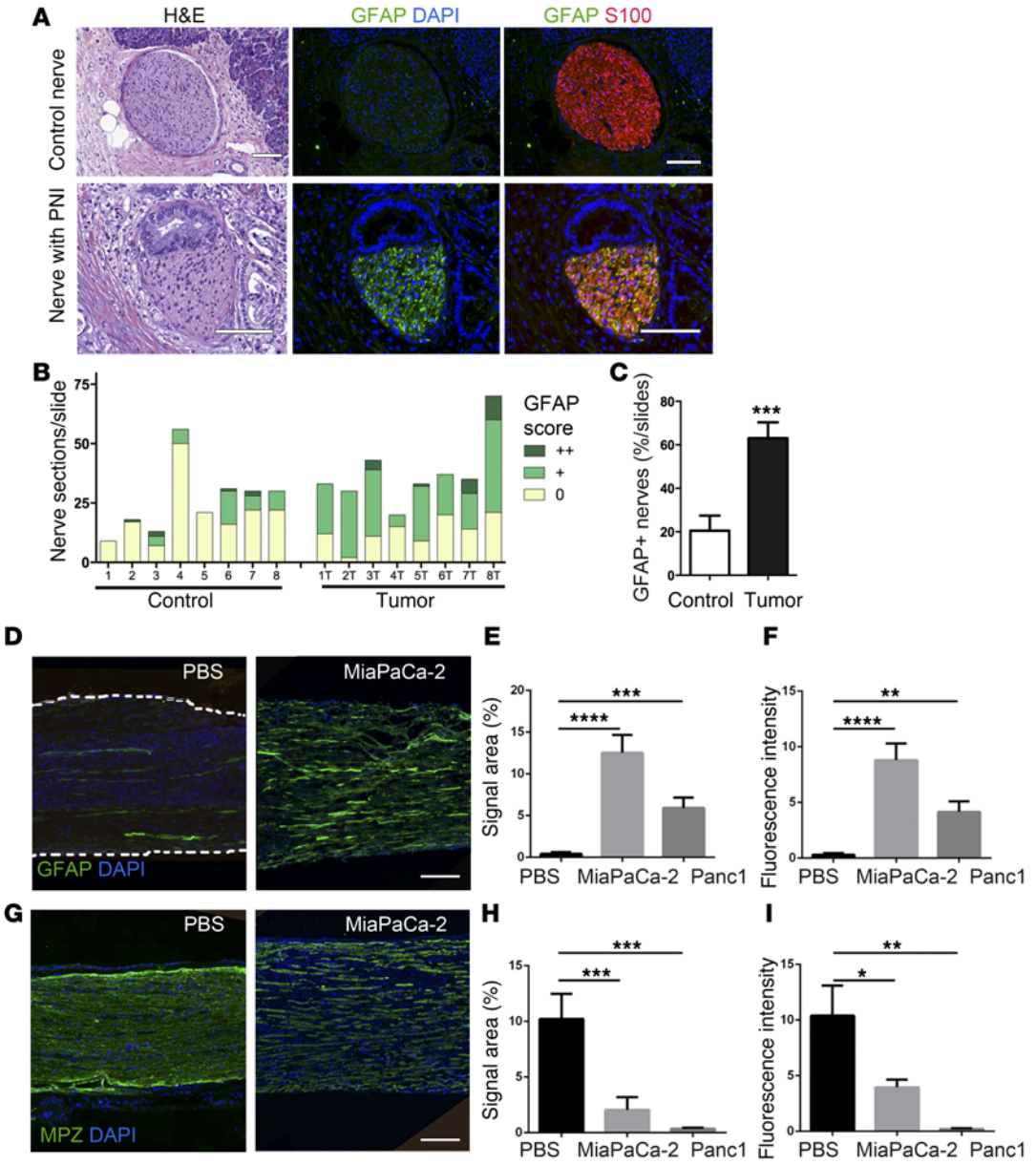

Figure 1. Increase of GFAP⁺ SCs in human and in murine perineural invasion specimens. (**A**) Representative images of nerve sections with GFAP (green) and S100 (red) staining in patients with adenocarcinoma pancreatic cancer and corresponding H&E sections. Control images are from a different tissue section from the same patient, taken in an area of the pancreas without cancer. Scale bar: 100 μm. PNI, perineural invasion specimens. (**B**) Quantification of nerves that scored negatively (0), moderately (+), or highly (++) for GFAP in 8 patients (numbered 1–8) in control and matched tumor sections. (**C**) Quantification of GFAP⁺ nerves (+ and ++) expressed by percentage per slide (n = 8). (**D**) A murine sciatic nerve injected with PBS or MiaPaCa-2 cells, showing increased levels of GFAP⁺ SCs in cancer cell–injected nerves. Immunofluorescence staining for GFAP (green) and nuclei (blue). Scale bar: 200 μm. (**E** and **F**) Quantification of GFAP⁺ SCs in PBS- (n = 23 images from 5 nerves), MiaPaCa-2 cell- (n = 13 images from 3 nerves), and Panc1 cell–injected sciatic nerves (n = 16 images from 3 nerves), as measured by (**E**) the area covered by GFAP signal and (**F**) the integrated fluorescent intensity. (**G**) Myelin protein zero (MPZ) staining in murine sciatic nerves injected with PBS or MiaPaCa-2 cells. Immunofluorescence staining for myelin protein zero (green) and nuclei (blue). Scale bar: 200 μm. (**H** and **I**) Quantification of myelin protein zero staining in PBS- (n = 15 images from 5 nerves), MiaPaCa-2 cell- (n = 15 images from 3 nerves), and Panc1 cell–injected sciatic nerves (n = 9 images from 3 nerves), as measured by area covered by (**H**) the myelin protein zero signal and (**I**) the integrated fluorescent intensity. Data represent mean ± SEM. *P < 0.05, **P < 0.01, ***P < 0.001, ****P < 0.0001, t test (**C**) or 1-way ANOVA with Holm-Sidak's multiple comparisons test (**E**, **F**, **H**, and **I**).

Schwann cells from the DRGs reduced the recruitment of both MiaPaCa-2 and Panc1 cells to neurites (Figure 4B). The addition of a nonneoplastic human Schwann cell line, HEI-286, which expresses GFAP (Supplemental Figure 4) and farnesylated GFP (F-GFP), to the radiated DRG led to an association of HEI-286 F-GFP cells with the neurites and a rescue of the DRG's ability to subsequently recruit MiaPaCa-2 cells to the neurites (Figure 4C). Collectively, these data demonstrate that dynamic Schwann cells actively recruit and lead cancer cells to neurites in the DRG coculture model, through heterocellular contact.

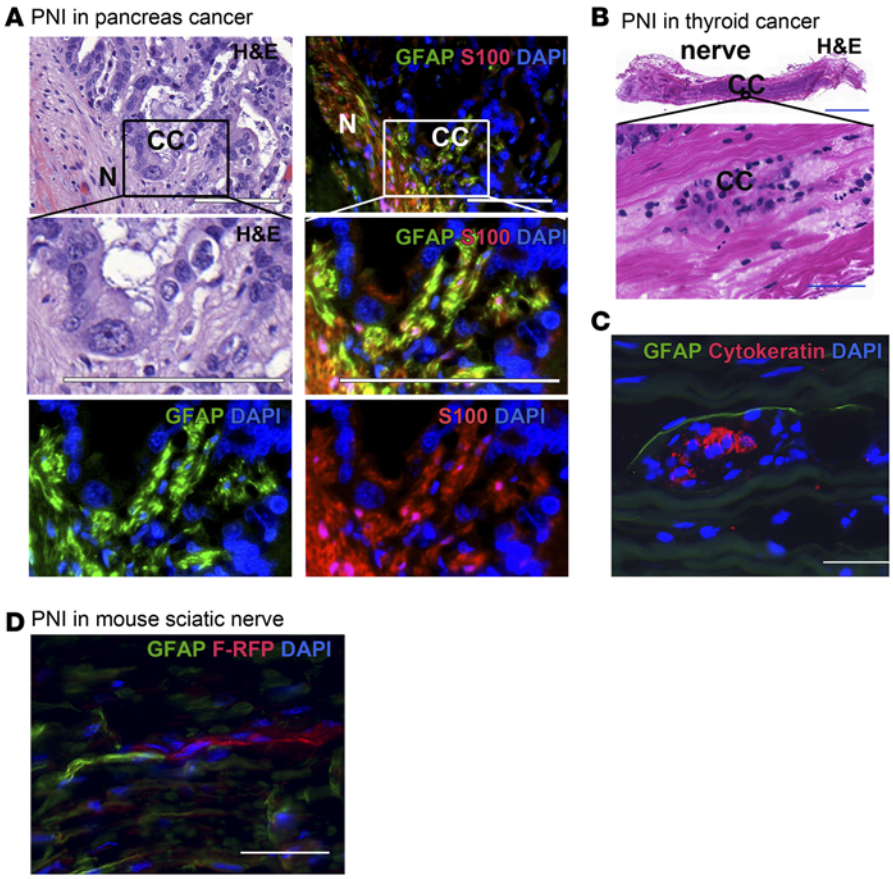

Figure 2. GFAP⁺ SCs associate with cancer cells in human and murine perineural invasion specimens. (**A**) GFAP⁺ SCs associate with cancer cells in nerves of patients with ductal pancreatic cancer. H&E staining and immunofluorescence staining for GFAP (green), S100 (red), and nuclei DAPI (blue) on transverse sections. GFAP⁺ SCs are enriched in the area next to the cancer cells (CC). Scale bar: 100 μm. N, nerve. (**B**) H&E staining of a longitudinal section of a segment of the recurrent laryngeal nerve from a patient with thyroid cancer. Cancer cell infiltration is shown at higher magnification. Scale bar: 2,000 μm (top image); 50 μm (bottom image). (**C**) Immunofluorescence staining for cytokeratin (red), GFAP (green), and nuclei DAPI (blue) showing GFAP⁺ SCs closely associated with a cluster of cancer cells (corresponding to bottom image in **B**). Scale bar: 50 μm. (**D**) Murine GFAP⁺ SCs associated with MiaPaCa-2 cancer cells expressing F-RFP. Immunofluorescence staining for GFAP (green) and nuclei (blue) on a longitudinal section of a murine sciatic nerve injected with MiaPaCa2 F-RFP cells. Scale bar: 50 μm.

Schwann cell contact reorganizes cancer cell clusters and promotes cell dispersion. We then created a model in which Schwann cells were the only nerve elements of the reconstructed microenvironment. To characterize Schwann cell and cancer cell behaviors upon contact and identify possible cellular mechanisms of cancer invasion, HEI-286 cells expressing F-GFP were cocultured in Matrigel with F-RFP MiaPaCa-2 and Panc1 cancer cells and imaged. Cancer cells in 3D Matrigel grew as spherical structures (Figure 5A). Interestingly, however, in the presence of Schwann cell contact two major events were induced: (a) dynamic reorganization of spherical structures into more linear chains of cells and (b) dissociation of individual cells from the cluster (Figure 5). To quantify the reorganization of spherical cell clusters into linear chains, we used a shape factor index, defined as $4\pi A/P^2$, with A standing for the area and P standing for the perimeter of the cancer cell cluster. This value approaches 1 when the shape is circular, and 0 when the shape is linear. The shape factor of the 3D cancer clusters decreased markedly when in contact with Schwann cells for MiaPaCa-2 (Figure 5A, from 0.44 ± 0.03 to 0.10 ± 0.01) and Panc1 (Supplemental Figure 5A, from 0.79 ± 0.03 to 0.39 ± 0.05). The shape factor was not affected when Schwann cells were present nearby or when they were when replaced by fibroblasts, suggesting that cancer cell contact with Schwann cells is necessary for this effect (Figure 5, A and B). The dynamic interactions between cancer cells and Schwann cells were observed by time-lapse microscopy and showed the formation of cancer cell chains (Figure 5B and Supplemental Video 2A) as well as the release of individual cancer cells from clusters (Figure 5B and Supplemental Video 2B). We noted that the Schwann cells were extremely dynamic compared with the cancer cells, making repetitive contact with individual cancer cells (Supplemental Video 2A). Such Schwann cell activity ultimately leads to a reorganization of cancer cell clusters and single-cell dispersion.

Schwann cell contact induces protrusive activity in cancer cells. To better visualize the interaction between Schwann cells and cancer cells, we performed time-lapse microscopy of 2D cocultures. MiaPaCa-2 cancer cells grown on top of a layer of Matrigel developed into circular monolayer clusters of cells (Figure 5C and Supplemental Video 3A). The subsequent addition of Schwann cells led to reorganization of cancer cell clusters into chains of cells, migration of cancer cells toward Schwann cells at sites of contact, and the dispersion of individual cancer cells from the clusters (Figure 5C and Supplemental Video 3, B and C). At sites of cell-cell contact, cancer cells developed protrusions directed toward Schwann cells, which determined the direction of cancer cell migration away from the colony (Figure 6A and Supplemental Video 3D). 64% of all contacts with a Schwann cell were associated with the formation of a protrusion in the cancer cell (80 of 125 total events). In contrast, only 14% of cancer cell protrusions were observed in the absence of Schwann cell contact during the 24-hour period of the video. The duration between contact and the formation of a protrusion was variable, from 10 to 290 minutes, with an average of 169 minutes ± 67 minutes (n = 8).

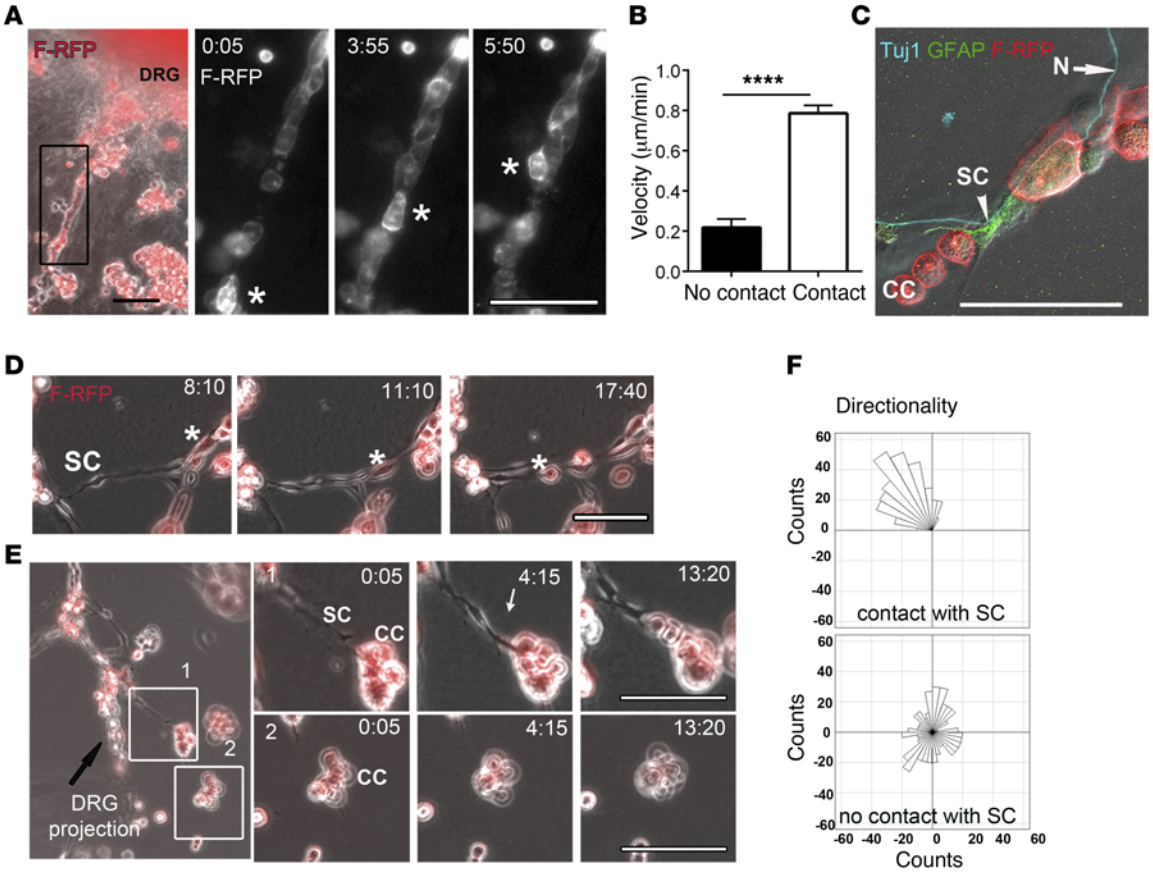

Figure 3. Schwann cells recruit cancer cells to DRG neurites. (**A**) Coculture of DRGs with MiaPaCa-2 F-RFP cells. Images from a time-lapse video showing progression of a cancer cell (marked by an asterisk) toward the center of the DRG (see Supplemental Video 1A). Times are shown as hours and minutes. (**B**) Cancer cells in contact with DRGs move faster than those not in contact. Quantification of the instantaneous velocity of MiaPaCa-2 cells without (n = 7) and with (n = 5) DRG contact. Data represent mean ± SEM. ****P < 0.0001, Mann Whitney test. (**C**) Association of Schwann cells with cancer cells on DRGs. Confocal image of a coculture of DRGs and MiaPaCa-2 F-RFP (red) cells immunostained for GFAP (green) and Tuj1 (blue), showing a Schwann cell with protrusions surrounding MiaPaCa-2 cells. The arrow marks a neuron element and the arrowhead marks a Schwann cell. (**D** and **E**) Images from time-lapse videos showing dynamic interactions between cancer cells and Schwann cells: (**D**) a cancer cell (marked by an asterisk) moving along Schwann cells (see Supplemental Video 1B) and (**E**) a DRG projection bridged (inset 1) or not bridged (inset 2) via Schwann cells to a cancer cell. Time-lapse images corresponding to inset 1 show cancer cell recruitment to the DRG. Time-lapse images corresponding to inset 2 show absence of cancer cell recruitment to the DRG. The arrow shows a protrusion developing from a cancer cell at a contact point with a Schwann cell. Times are shown as hours and minutes (see Supplemental Video 1, C and D). (**F**) Quantification of directionality of cancer cell movements corresponding to time-lapse videos shown in **E** after tracking cells over 24 hours, showing unidirectional migration by cancer cells toward their associated Schwann cells (top) (n = 6 cells) and random migration of cancer cells not associated with Schwann cells (bottom) (n = 8 cells). Scale bar: 100 μm.

Schwann cells intercalate into cancer cell clusters, disrupting cell-cell contacts. Protrusions formed by cancer cells at sites of Schwann cell contact were not sufficient to allow for cancer cell dispersion from a cluster. Time-lapse experiments revealed that cancer cell dissociation most often required Schwann cell intercalation among cancer cells within a cluster (Figure 6B and Supplemental Video 3C). Schwann cells intercalated between cancer cells via long protrusions, interrupting cell-cell contacts (Figure 6B, see empty arrows) and facilitating their dissociation from the cluster. Of the contact events between Schwann cells and cancer cells that led to cancer cell protrusions, 93% of these events failed to show any subsequent cancer cell dissociation. However, in 6% of these events, we observed Schwann cell intercalation and cancer cell dissociation. In just 1% of these events, we observed cancer cell dissociation, without any discernible Schwann cell intercalation (Figure 6C and Supplemental Video 3E). Therefore, the specific sequence of Schwann cell contact, cancer cell protrusion, and Schwann cell intercalation between adjacent cancer cells most frequently led to individual cancer cell dissociation and dispersion from the cluster.

Contact between cancer cells and Schwann cells promotes cancer cell invasion. We next assessed whether Schwann cell contact with cancer cells may directly affect cancer invasion. We developed a quantitative 3D invasion assay. HEI-286 cells expressing F-GFP were cultured in Matrigel for 6 days, and red fluorescent cancer cells were then added on top of a cube of Matrigel. Under these conditions, Schwann cells and cancer cells were in direct contact with each other at the top of Matrigel (Figure 7). Three days later, the number of cancer cells invading the Matrigel was measured by 3D analysis of confocal images. The presence of Schwann cells

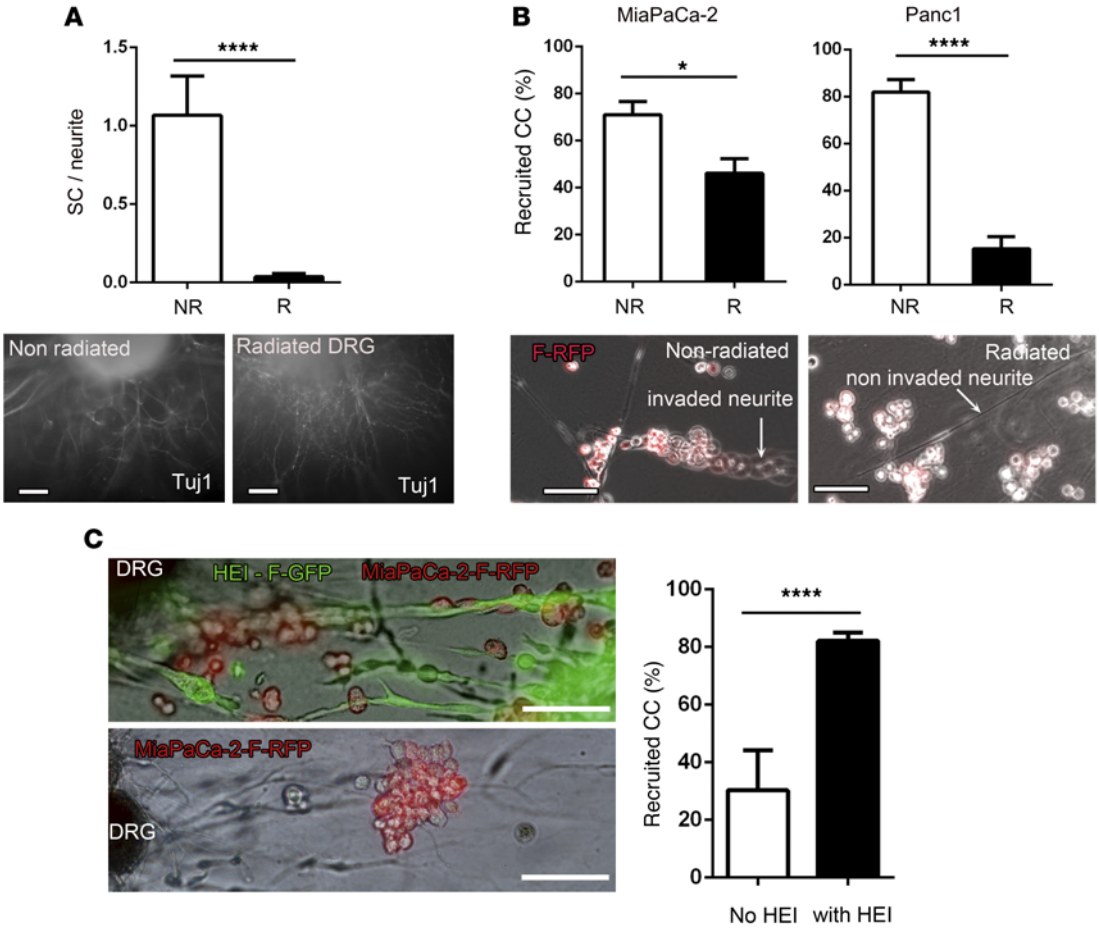

Figure 4. Depletion of Schwann cells inhibits recruitment of cancer cells to DRG projections. (**A**) Radiation treatment of DRGs reduces the number of associated Schwann cells. Quantification of the number of Schwann cells on neurites from radiated (R) (n = 22) and nonradiated (NR) DRGs (n = 16). Immunofluorescence staining for Tuj1 shows viable neurites. (**B**) Radiation treatment of DRGs decreases cancer cell recruitment to DRGs. Quantification of recruitment of MiaPaCa-2 and Panc1 cells to DRGs (n = 5 in nonradiated DRGs and n = 4 in radiated DRGs). Microscopic examination of the recruitment of cancer cells (red) to radiated and nonradiated DRGs. Images show MiaPaCa-2 F-RFP cells. (**C**) Addition of HEI-286 cells to irradiated DRGs increases cancer cell recruitment to the neurites. Microscopic examination of the recruitment of MiaPaCa-2 F-RFP cells to irradiated DRGs with and without HEI-286 F-GFP cells. Quantification of the recruitment of MiaPaCa-2 cells to irradiated neurites in the presence (n = 18) or absence (n = 14) of HEI-286 cells. Data represent mean ± SEM. $^*P < 0.05$, $^{****}P < 0.0001$, t test. Scale bar: 100 μm.

increased cancer cell invasion by 10-fold, as compared with Matrigel without the presence of Schwann cells, or 4-fold, as compared with fibroblasts embedded in the Matrigel (Figure 7B).

To assess whether soluble factors released by Schwann cells are responsible for this effect, invasion was also measured either in the presence of Schwann cell–conditioned medium generated from HEI-286 cells or with Schwann cells grown on the bottom of the Matrigel chamber with no direct cell contact. No significant invasion was detected with conditioned medium or in the absence of cell-cell contact (Figure 8A).

We noted that Schwann cells form tunnels in 3D Matrigel, as seen in time-lapse videos (Supplemental Figure 6A), and it has been reported that fibroblasts also form tunnels in matrix and that this facilitates carcinoma cell invasion (8). To test whether Schwann cell–derived tunnels themselves can facilitate invasion, Schwann cells were eliminated using puromycin 6 days after seeding into Matrigel. Puromycin did not affect the viability of cancer cells in these assays, because puromycin-resistant MiaPaCa-2 cells were generated and used for these studies. In addition, their ability to invade was not altered in the presence or absence of puromycin, as tested using puromycin-resistant HEI-286 cells (Supplemental Figure 6B). Schwann cells secrete laminin, which coats the tunnels and was visualized by immunofluorescence both when Schwann cells were alive and when Schwann cells were removed after puromycin treatment (Supplemental Figure 6C). The level of cell invasion after Schwann cell death following puromycin treatment was approximately one-third that in the control group, suggesting that the tunnels formed by Schwann cells could not account for the increased invasion seen in the presence of Schwann cells. Furthermore, the addition of Schwann cell–conditioned medium to these tunnels did not promote cancer cell invasion (Figure 8B). Collectively, these data demonstrate that direct contact between Schwann cells and cancer cells is necessary to promote efficient cancer cell invasion in a 3D gel matrix.

Depletion of NCAM1 in Schwann cells decreases cancer cell invasion in vitro. To explore potential factors that affect how

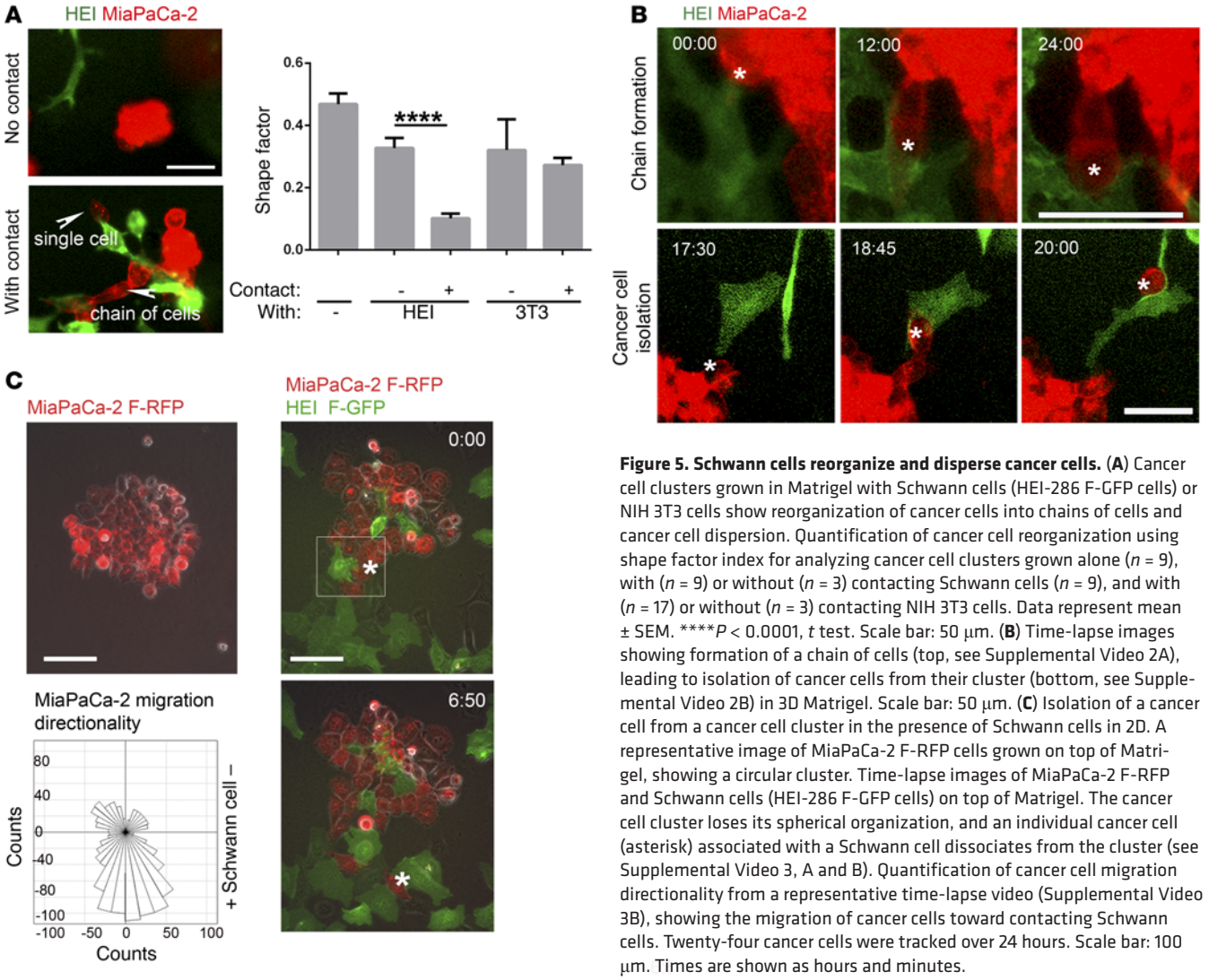

Figure 5. Schwann cells reorganize and disperse cancer cells. (**A**) Cancer cell clusters grown in Matrigel with Schwann cells (HEI-286 F-GFP cells) or NIH 3T3 cells show reorganization of cancer cells into chains of cells and cancer cell dispersion. Quantification of cancer cell reorganization using shape factor index for analyzing cancer cell clusters grown alone (n = 9), with (n = 9) or without (n = 3) contacting Schwann cells (n = 9), and with (n = 17) or without (n = 3) contacting NIH 3T3 cells. Data represent mean ± SEM. ****$P < 0.0001$, t test. Scale bar: 50 μm. (**B**) Time-lapse images showing formation of a chain of cells (top, see Supplemental Video 2A), leading to isolation of cancer cells from their cluster (bottom, see Supplemental Video 2B) in 3D Matrigel. Scale bar: 50 μm. (**C**) Isolation of a cancer cell from a cancer cell cluster in the presence of Schwann cells in 2D. A representative image of MiaPaCa-2 F-RFP cells grown on top of Matrigel, showing a circular cluster. Time-lapse images of MiaPaCa-2 F-RFP and Schwann cells (HEI-286 F-GFP cells) on top of Matrigel. The cancer cell cluster loses its spherical organization, and an individual cancer cell (asterisk) associated with a Schwann cell dissociates from the cluster (see Supplemental Video 3, A and B). Quantification of cancer cell migration directionality from a representative time-lapse video (Supplemental Video 3B), showing the migration of cancer cells toward contacting Schwann cells. Twenty-four cancer cells were tracked over 24 hours. Scale bar: 100 μm. Times are shown as hours and minutes.

Schwann cells behave with cancer cells, we considered the immunoglobulin family member neural cell adhesion molecule 1 (NCAM1). NCAM1 expression has been correlated with the presence of perineural invasion in specimens from a variety of cancers (28–34) and has been reported to play a role in cancer progression and axon guidance (35–41).

Three different shRNAs targeting NCAM1 (referred to herein as sh 1, sh 2, and sh 3, respectively) were used to generate stable cell lines in HEI-286 Schwann cells, and Western blot and immunofluorescence analysis revealed that sh 1 and sh 2 caused strong depletion, while sh 3 led to intermediate depletion of the 140-kDa NCAM1 isoform (Figure 9A and Supplemental Figure 7A). The proliferation of NCAM1-depleted HEI-286 cells and their ability to migrate and form tunnels in Matrigel remained intact (Figure 9B and Supplemental Figure 7, B and C). The 3D invasion assay showed a 50% to 60% decrease in cancer cell invasion when Schwann cells expressing sh 1 or sh 2 were used and only a small effect with sh 3–expressing cells (Figure 9, B and C). Overexpressing NCAM1 in NIH 3T3 fibroblasts grown in Matrigel did not increase cancer invasion (Supplemental Figure 8). The decreased cancer invasion seen with the NCAM1-depleted HEI-286/sh 2 cells could be partially rescued by expression of RNAi-resistant chicken NCAM1 (Figure 9, D and E). Chicken NCAM1 may not functionally recapitulate all aspects of human NCAM1. We also investigated the effect of NCAM1 depletion in Schwann cells on cancer cell interactions at sites of contact. Depletion of NCAM1 led to a significant decrease in the ability of Schwann cells to affect the shape of cancer cell clusters and to promote cancer cell protrusions (Figure 9, F and G).

We then assessed the ability of NCAM1-depleted HEI-286 Schwann cells to recruit cancer cells in radiated DRGs and observed a significant decrease of MiaPaCa-2 cell recruitment at the neurites (Supplemental Figure 9). These findings demonstrate that NCAM1 expression by Schwann cells enables cell behavior that facilitates the disruption of cancer cell clusters, recruitment of cancer cells, and promotion of invasion.

NCAM1 expression in Schwann cells upon contact with tumor cells. We investigated NCAM1 expression in human pancreatic adenocarcinoma specimens. NCAM1 was expressed by Schwann cells that were in contact with cancer cells (Figure 10A), and these cells were also GFAP$^+$ (Figure 10B). We then cocultured HEI-286 Schwann cells, expressing either NCAM1-GFP or F-GFP, with MiaPaCa-2

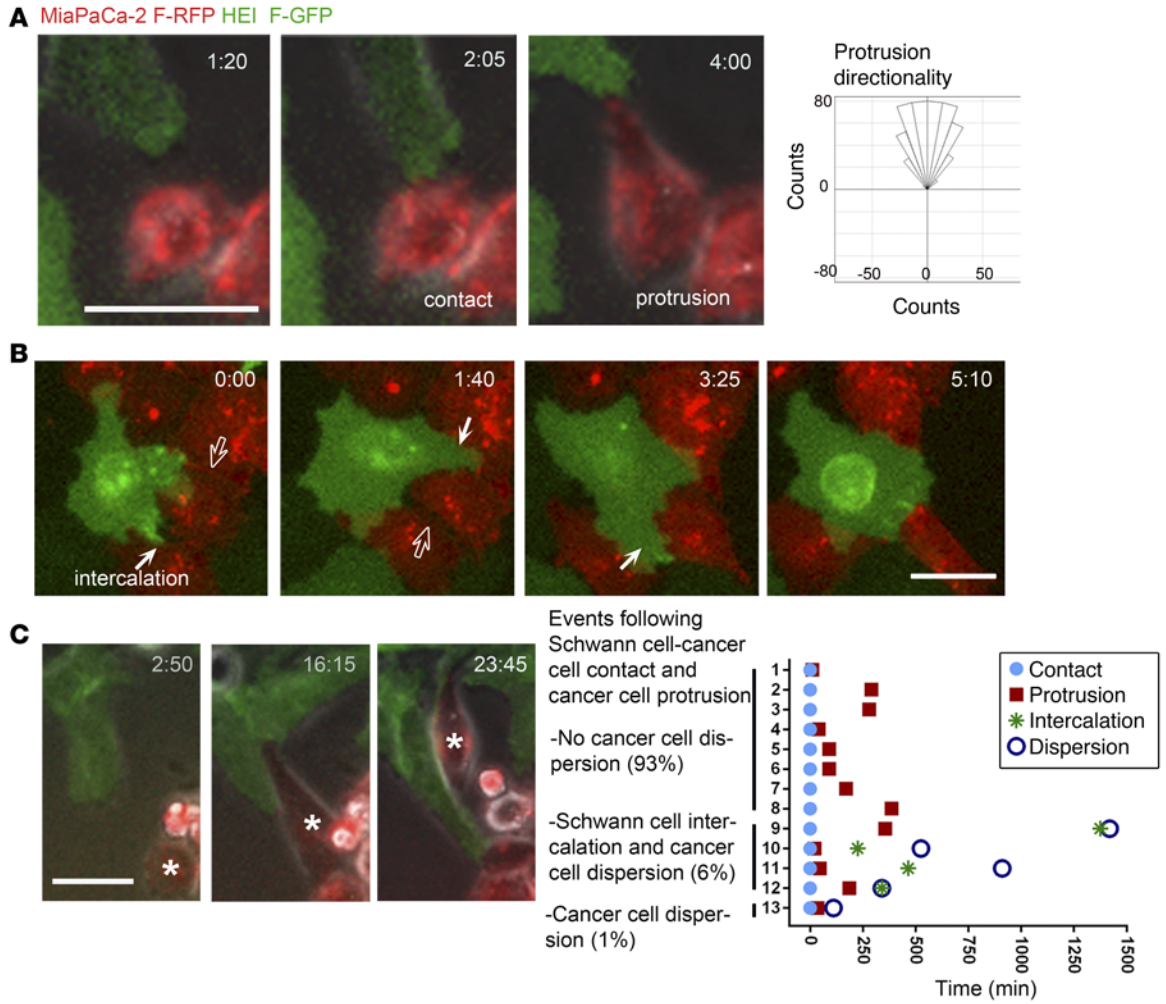

Figure 6. Schwann cells induce cancer cell protrusions and intercalate between cancer cells. (**A**) Heterocellular contact induces protrusions in cancer cells. Time-lapse images of dynamic interactions of MiaPaCa-2 cells and a Schwann cell showing heterocellular contact and the formation of a cancer cell protrusion directed toward the Schwann cell (see Supplemental Video 3D). Quantification of cancer cell protrusion directionality measured on cancer cells with one site of contact with Schwann cells at a time. The images were rotated with the superior *y* axis representing the Schwann cell position on the image in which the Schwann cell and cancer cell were in contact before the formation of protrusion (n = 8 cells). (**B**) Schwann cells intercalate between cancer cells. Time-lapse images showing Schwann cell protrusions intercalating between cancer cells. The image at time 0:00 corresponds to the indicated boxed area in Figure 5C. White arrows show Schwann cell protrusions. Empty arrows show cancer cell–cancer cell contacts. Note weaker cancer cell–cancer cell contact at time 1:40 after Schwann cell intercalation and a stronger cancer cell–cancer cell contact at time 0:00 before intercalation (see Supplemental Video 3C). (**C**) The sequence of events – contact, protrusion, intercalation, and migration. Images show cancer cell (asterisk) dissociation after Schwann cell intercalation (see Supplemental Video 3E). The timeline of events after heterocellular contact and subsequent formation of cancer cell protrusion shows sequence and frequency of following events: contact, protrusion, intercalation, and migration (total n of events = 80). Although protrusions occur frequently after contact, migration mostly occurs after intercalation. Numbers along the *y* axis refer to events following Schwann cell–cancer cell contact and cancer cell protrusion. Scale bar: 50 μm. Times are shown as hours and minutes.

F-RFP cells. NCAM1-GFP localized to the HEI-286 plasma membrane and accumulated in areas in which long filopodia extend outward, contacting cancer cells and other Schwann cells. In contrast, F-GFP was homogeneously distributed at the plasma membrane of HEI-286 cells (Figure 10C, top images). Interestingly, cocultured NCAM1-GFP–expressing HEI-286 and NCAM1-expressing MiaPaCa-2 cells form long filopodia that contain NCAM1 and intertwine at sites of contact (Figure 10C, right bottom image). These results suggest that NCAM1 is likely functioning at cell-cell contact sites via filopodia when overexpressed in these cell lines.

Loss of NCAM1 decreases cancer cell invasion in vivo. To assess the role of NCAM1 in an in vivo model of perineural invasion, we injected murine pancreatic cancer cells, Panc02-H7, into the sciatic nerves of WT or NCAM1 KO mice and assessed nerve invasion by sciatic nerve extraction and H&E staining of longitudinal sections. The time course of sciatic nerve invasion is rapid in this syngeneic model of perineural invasion, as previously described (42). Histological analysis revealed decreased invasion in NCAM1 KO mice, as measured by the distribution (length and area) of cancer cell invasion (Figure 11A), consistent with the concept that NCAM1 expression in Schwann cells supports cancer cell invasion into the nerve. NCAM1 is present in cell types other than Schwann cells, and we cannot exclude the possibility that the depletion of NCAM1 in other cell types may have contributed to the effects observed in NCAM1 KO mice.

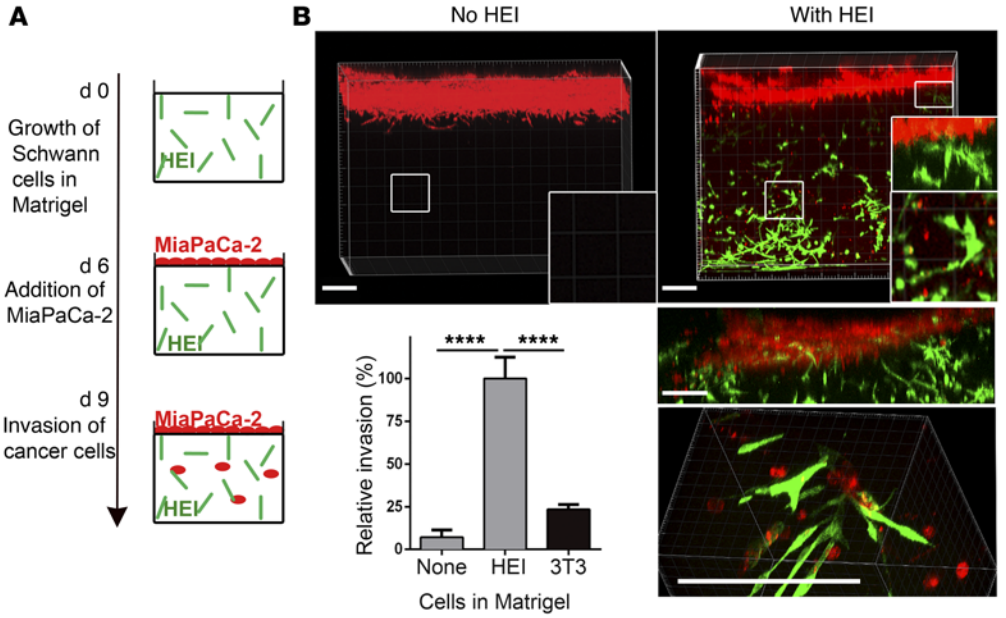

Figure 7. Schwann cells promote cancer cell invasion. (**A**) Schematic of the 3D invasion assay. HEI-286 F-GFP Schwann cells were grow in Matrigel for 6 days before addition of MiaPaCa-2 F-RFP cells to the top of the Matrigel, where contact between Schwann cells and cancer cells can occur. Invasion was measured 3 days later by 3D analysis of confocal images and (**B**) is shown via 3D representations of Z-stacks of confocal images. Cancer cell invasion in the absence and presence of Schwann cells seeded at 70 cells per μl of Matrigel. The rectangular inset shows contact of Schwann cells (green) with cancer cells (red) at the top of the Matrigel, and the square insets indicate extent of invasion in absence and presence of Schwann cells. The middle image shows contact between MiaPaCa-2 and Schwann cells at the top of Matrigel, and the bottom image shows association between Schwann cells and MiaPaCa-2 cells at higher magnification. Quantification of cancer cell invasion in Matrigel seeded in the absence (n = 4) or presence of Schwann cells (n = 8) or NIH 3T3 cells (n = 8). Data represent mean ± SEM. ****$P < 0.0001$, 1-way ANOVA with Holm-Sidak's multiple comparisons test. Scale bar: 200 μm.

In addition, we assessed whether NCAM1 depletion prevents the dedifferentiation of Schwann cells into GFAP$^+$ cells in sciatic nerves injected with cancer cells using immunofluorescence staining. The Schwann cell GFAP signal was expressed equally in the invaded sciatic nerves of NCAM1 KO mice and WT mice, suggesting that NCAM1 does not play a role in the dedifferentiation process of the Schwann cells (Figure 11B).

To assess the clinical manifestation of perineural invasion in WT and NCAM1 KO mice, sciatic nerve function was monitored and quantified using a previously described scoring system (21); a score of 4 indicated fully intact hind limb motor function, and a score of 1 indicated complete hind limb paralysis. WT mice developed rapid paralysis, detected as early as 3 days after nerve injection with cancer cells, while mice injected with PBS retained fully intact function. In contrast, the NCAM1 KO mice retained partial sciatic nerve function after cancer cell injection. Together, these studies demonstrate an important role for NCAM1 expression by the host microenvironment in directing migration of cancer cells through cell-cell interactions and in facilitating the development of clinical manifestations of perineural invasion in vivo (Figure 11C).

Discussion

The nerve microenvironment actively facilitates cancer progression for numerous different cancer types. Elucidating the cellular and molecular basis of nerve participation in the process of cancer invasion and identifying the cells involved in this process are essential to develop therapeutic approaches. Here, we describe a cellular mechanism which we believe to be novel, through which Schwann cells facilitate cancer cell invasion. These results highlight the importance of heterocellular contact and cancer cell dispersion as key events that collectively promote cancer invasion of nerves. This process is dependent on NCAM1 expression by Schwann cells. The clinical relevance of these findings is supported by the detection of an association between activated Schwann cells and cancer cells in human perineural invasion specimens.

A cellular mechanism of cancer dispersion. This study identifies Schwann cells as a cell type in the microenvironment that participates in cancer cell invasion and characterizes a mechanism of cancer dispersion that has not been previously reported. Prior studies have shown that interactions of cells of the microenvironment and cancer cells contribute to cancer invasion by modification of the extracellular matrix and paracrine signaling (5, 8). Live-imaging data revealed the ability of Schwann cells to degrade matrix and form tunnels in Matrigel. These tunnels could served as tracks for the cancer cells and are reminiscent of the bands of Bungner, the tracks formed by Schwann cells involved in axon guidance. Importantly, we demonstrate that neither the empty tunnels formed by Schwann cells nor soluble factors released by Schwann cells are sufficient to induce cancer invasion. The physical contact between live Schwann cells and cancer cells is required for the enhancement in cancer invasion. We cannot exclude the possibility that chemokines may be induced after contact between a Schwann cell and a cancer cell to promote cancer invasion or that membrane-bound chemokines may be involved in Schwann cell–facilitated cancer invasion. Studies have revealed the expression of CX3CL1, a chemokine that can be soluble or membrane bound, and its receptor CX3CR1 in perineural invasion specimens in pancreatic cancer (43), in gastric carcinoma (44), and in squamous cell carcinoma of the tongue (45).

A few studies have previously demonstrated that contact between cells of the microenvironment and cancer cells may promote cancer spread (46, 47). One study demonstrates that the interaction between breast cancer cells and bone marrow stromal cells via cadherin-11 facilitates cancer invasion (43). Another study reports that the physical interaction between macrophages and breast cancer cells correlates with invasion and invadopo-

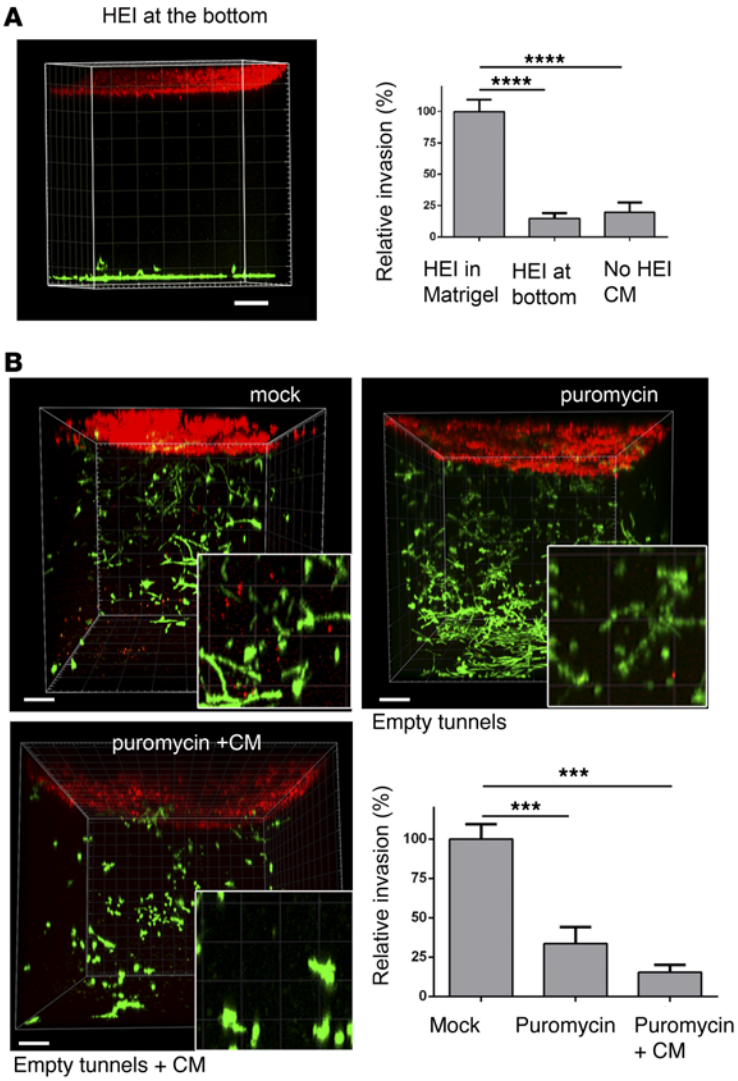

Figure 8. Schwann cell promotion of cancer cell invasion is contact dependent. (**A**) Schwann cell–conditioned medium (CM) is not sufficient to induce invasion. Representative Z-stack of confocal images and quantification (n = 4 per condition) showing absence of cancer cell invasion when Schwann cells are seeded at the bottom of the dish in the absence or presence of Schwann cell–conditioned medium. (**B**) Empty tunnels formed by Schwann cells are not sufficient to induce cancer cell invasion. Representative Z-stacks of confocal images showing Schwann cell–dependent cancer cell invasion in presence of tunnels with Schwann cells, in presence of tunnels without Schwann cells (puromycin treatment), and in presence of tunnels without Schwann cells but with conditioned medium. Quantification of cancer cell invasion (n = 4 for each group). Data represent mean ± SEM. ***P < 0.001, ****P < 0.0001, 1-way ANOVA with Holm-Sidak's multiple comparisons test. Scale bar: 200 μm.

dium formation in cancer cells (42). In this study, live imaging reveals that at Schwann cell and cancer cell contact, Schwann cells are very dynamic and (a) induce cancer cell protrusions at points of contact, (b) intercalate between cancer cells, (c) act as leader cells to trailing cancer cells, (d) reorganize cancer cell clusters, and (e) ultimately disperse single cancer cells away from neighboring cells, facilitating perineural invasion. These data provide a descriptive analysis of the complex behavior of Schwann cells in promoting cancer invasion.

NCAM1 expression in Schwann cells promotes perineural invasion. Previous studies have proposed a role for NCAM1 in perineural invasion. These studies are based on correlations between NCAM1 expression in cancer cells, as seen in histologic specimens, and perineural invasion (29–33). Elevated NCAM1 expression has also been reported in nerves at sites of perineural invasion (48). We demonstrate here that NCAM1 plays a role in Schwann cell–facilitated cancer cell invasion. Importantly, NCAM1 KO mice developed less perineural invasion and a slower progression of sciatic nerve paralysis as compared with WT mice. NCAM1 has known roles in supporting neuronal outgrowth and axonal guidance (36, 38–40). NCAM1-dependent cancer cell protrusion formation following Schwann cell contact appears to show similarities with NCAM1-dependent outgrowth of neurites. In the case of nerve repair, NCAM1 appears to function as a signaling molecule, rather than an adhesion molecule (40), and activates the FGF receptor/PLCγ/PKC and the Ras/MAP kinase pathways (38, 49). It is possible that NCAM1 mediates the activation of the same signaling molecules in cancer cells and in the neuron-like cells, in which these molecules have a known role in cancer progression (50–53). Interestingly, interplay between E-cadherin and NCAM1 has been proposed in cancer cells (54, 55). The loss of E-cadherin during epithelial-to-mesenchymal transition in cancer may be associated with an upregulation of NCAM1. With E-cadherin expression, the low levels of NCAM1 are localized outside of the lipid raft and associate with the FGF receptor. However, when E-cadherin is repressed, NCAM1 is upregulated and a subset is localized in the lipid rafts, in which it associates with $p59^{Fyn}$, whose subsequent activation leads to inhibition of focal adhesion assembly and an increase in cancer cell migration (54). Another study reported that pancreatic cancer cell lines with oncogenic K-ras have increased expression levels of polysialylated NCAM1, which interacts with E-cadherin to create sterical hindrance of homophilic binding and diminish cellular adhesion (55). Further studies are necessary to clarify the role of NCAM1 on cancer cells during the Schwann cell–facilitated cancer cell invasion.

Contact between Schwann cells and cancer cells is not prevented when NCAM1 is depleted from Schwann cells, but the protrusions formed by cancer cells are less frequent and their directional movement toward the Schwann cells is diminished. Although NCAM1-mediated adhesion might not be necessary for initial cell-cell contact, it likely is involved in guidance dynamics. When a Schwann cell retracts after contact with a cancer cell, the newly formed cancer cell protrusion might theoretically remain connected to the Schwann cell through NCAM1 interactions enabling it to follow the Schwann cell.

The role that NCAM1 plays in Schwann cell and cancer cell interactions may be more complex than homophilic binding. Cancer cells in contact with NCAM1-expressing Schwann cells in human specimens of pancreatic adenocarcinomas did not express detectable levels of NCAM1, as shown by immunofluorescence.

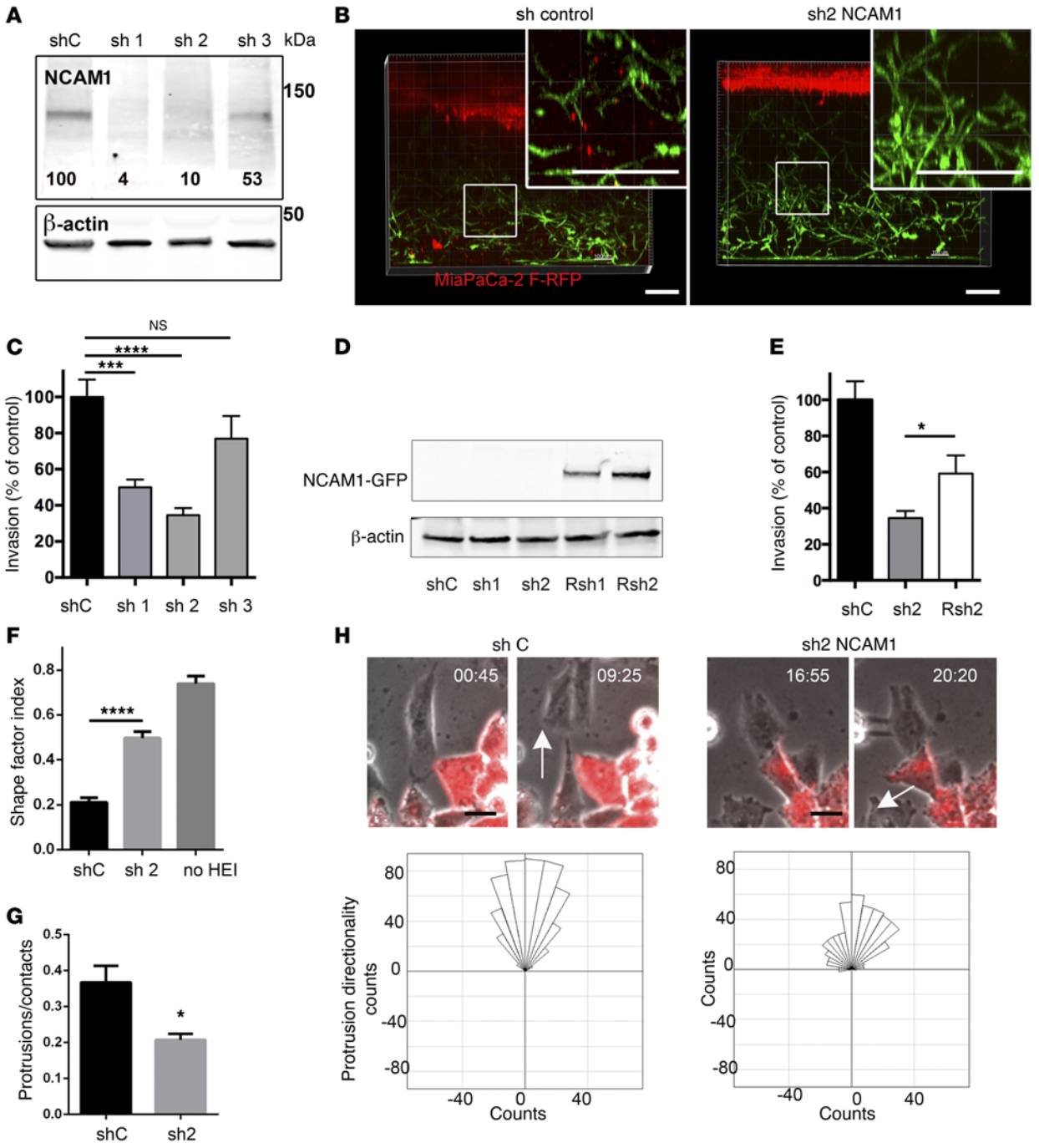

Figure 9. NCAM1 expression by Schwann cells promotes cancer cell invasion in vitro. (**A**) NCAM1 depletion in Schwann cells (HEI-286). Western blot analysis in control (shC) and NCAM1 shRNA–expressing cells. NCAM1 was strongly depleted in cell lines infected with sh 1 and sh 2 constructs and mildly depleted with sh 3. (**B** and **C**) NCAM1 depletion reduced cancer cell invasion. Representative Z-stacks of confocal images and quantification showing cancer cell invasion in control shRNA– and NCAM1 shRNA1–expressing Schwann cells. n = 16 (shC), n = 8 (sh 1), n = 20 (sh 2), n = 8 (sh 3). Scale bar: 200 μm. (**D** and **E**) Cancer cell invasion rescue in NCAM1-depleted cells with chicken NCAM1-GFP expression. Western blot analysis in control cells (shC), NCAM1-depleted cells (sh 1, sh 2), and NCAM1-depleted cells plus chicken GFP-NCAM1 (Rsh 1, Rsh 2). Quantification of cancer cell invasion in presence of control Schwann cells (shC), NCAM1-depleted Schwann cells (sh 2), and NCAM1-depleted Schwann cells expressing chicken NCAM1 (Rsh 2). n = 16 (shC), n = 20 (sh 2), n = 8 (Rsh 2). (**F**) NCAM1-depleted Schwann cells are less efficient than control Schwann cells in reorganizing circular cancer cell cluster. Quantification of reorganization of cancer cell clusters contacting control Schwann cells or NCAM1-depleted Schwann cells (sh 2) or in absence of Schwann cells (no HEI) using shape factor index. n = 15 (shC), n = 16 (sh 2). (**G**) NCAM1-depleted Schwann cells are less efficient than control Schwann cells in inducing cancer cell protrusions. n = 4 experiments with >45 contacts/experiment/condition. (**H**) Upon contact with NCAM1-depleted Schwann cells, cancer cells develop protrusions with a defect in their directionality. Images from time-lapse videos and Rose diagrams showing quantification of directionality of cancer protrusions (arrows) after contact with Schwann cell as done in Figure 5 (n = 9 cells). Times are shown as hours and minutes. Scale bar: 20 μm. Data represent mean ± SEM. *P < 0.05,***P < 0.0001, ****P < 0.0001, t test (**G**) or 1-way ANOVA with Holm-Sidak's multiple comparisons test (**C**, **E**, and **F**).

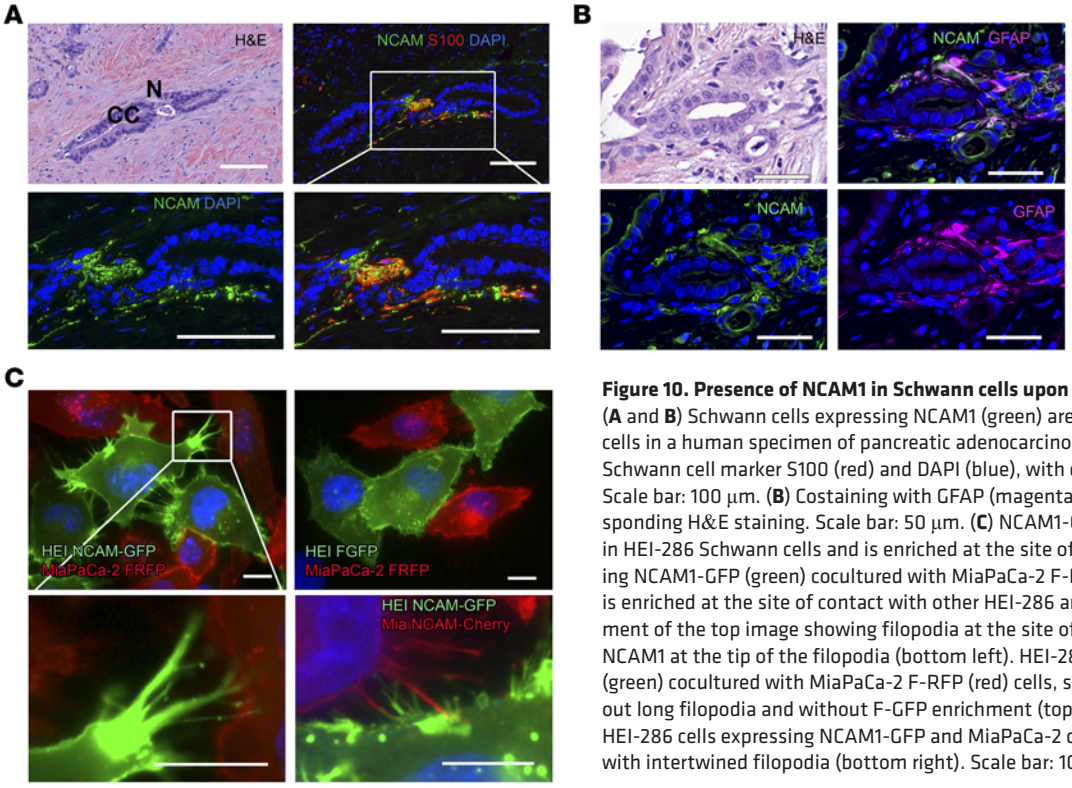

Figure 10. Presence of NCAM1 in Schwann cells upon contact with tumor cells. (**A** and **B**) Schwann cells expressing NCAM1 (green) are found in contact with cancer cells in a human specimen of pancreatic adenocarcinoma. (**A**) Costaining with the Schwann cell marker S100 (red) and DAPI (blue), with corresponding H&E staining. Scale bar: 100 μm. (**B**) Costaining with GFAP (magenta) and DAPI (blue), with corresponding H&E staining. Scale bar: 50 μm. (**C**) NCAM1-GFP induces filopodia formation in HEI-286 Schwann cells and is enriched at the site of contact. HEI-286 cells expressing NCAM1-GFP (green) cocultured with MiaPaCa-2 F-RFP (red) cells (top left). NCAM1 is enriched at the site of contact with other HEI-286 and MiaPaCa-2 cells. Enlargement of the top image showing filopodia at the site of contact and enrichment of NCAM1 at the tip of the filopodia (bottom left). HEI-286 cells expressing F-GFP (green) cocultured with MiaPaCa-2 F-RFP (red) cells, showing zones of contact without long filopodia and without F-GFP enrichment (top right). Zone of contact between HEI-286 cells expressing NCAM1-GFP and MiaPaCa-2 cells expressing NCAM1-Cherry with intertwined filopodia (bottom right). Scale bar: 10 μm.

It is possible that some of the NCAM1-mediated effects result from heterophilic rather than homophilic interactions or that the expression of NCAM1 in cancer cells may be dynamically upregulated or downregulated. NCAM1 expression can also be stimulated by secreted factors such as TNF-α (56). NCAM1 KO Schwann cells were still able to make contact with cancer cells, although their ability to recruit cancer cells was diminished. NCAM1 expression by Schwann cells therefore enables its cancer-promoting behavior.

Schwann cells dedifferentiated to GFAP-expressing cells in sciatic nerves invaded by cancer cells in NCAM1 KO mice around the tumor (Figure 11), demonstrating that the Schwann cell dedifferentiation program seen with nerve injury is not dependent on NCAM1. However, the NCAM1 KO mice were less susceptible to perineural invasion as compared with WT mice, and NCAM1 KO Schwann cells showed a diminished ability to disrupt cancer cell clusters and facilitate cancer invasion. The overexpression of NCAM1 in Schwann cells induces the formation of longer filopodia, consistent with the report of the formation of similar structures in other cell types (57, 58). Collectively, this information supports the following sequence of events: (a) Schwann cells adjacent to a site of cancer invasion dedifferentiate into GFAP$^+$ SCs, similar to their response to nerve injury, (b) NCAM1 is expressed in these Schwann cells and induces longer filopodia formation, and (c) dynamic GFAP$^+$ SCs contact cancer cells and initiate a process of cancer cluster dispersion and promotion of cancer invasion along nerves. The identification of the involvement of NCAM1 in Schwann cell–dependent cancer cell invasion provides insights into the process of cancer invasion.

Schwann cells may promote cancer invasion at sites where perineural invasion is not detected. Schwann cells are present not only in large caliber nerves but also in single-fiber neurons at the terminal endings of nerves. Highly innervated organs, such as the pancreas, prostate, and salivary glands, have abundant tiny nerves that terminate at glandular structures, and, furthermore, Schwann cells from single-fiber nerves of rat pancreas are found in contact with acini cells (59, 60). Schwann cells are therefore likely to be in close proximity to cancer cells at early stages of pancreatic cancer development and have an affinity for cancer cells (22). We speculate that Schwann cells might also facilitate cancer progression in this setting. This possibility is supported by recent reports showing a reduction of tumor spreading after organ denervation in prostate and gastric cancer (1, 2) and the detection of Schwann cells at premalignant stages of tumor specimens (22). The ability of Schwann cells to promote cancer cell dispersion suggests that Schwann cells might also play a role in promoting cancer invasion at any site where these two cell types may come into direct contact.

Normal functions of Schwann cells are involved in perineural invasion. Interestingly, this elaborate Schwann cell behavior that facilitates cancer invasion shares many strong similarities with normal Schwann cell processes observed in neurobiology. During human fetal development, Schwann cells isolate individual axons from large bundles by invaginating between individual axons to separate them from each other (11, 61). Here, we showed that Schwann cells exhibit a similar behavior by intercalating between cancer cells. Schwann cells are also known to play an important role during nerve repair by inducing and guiding axonal extensions (12, 13, 15, 16, 62). Our time-lapse images show that Schwann cells can also guide cancer cells toward neurites through the promotion of protrusions. The formation of directed protrusions guides cancer cells away from neighboring cancer cells, which is a process remi-

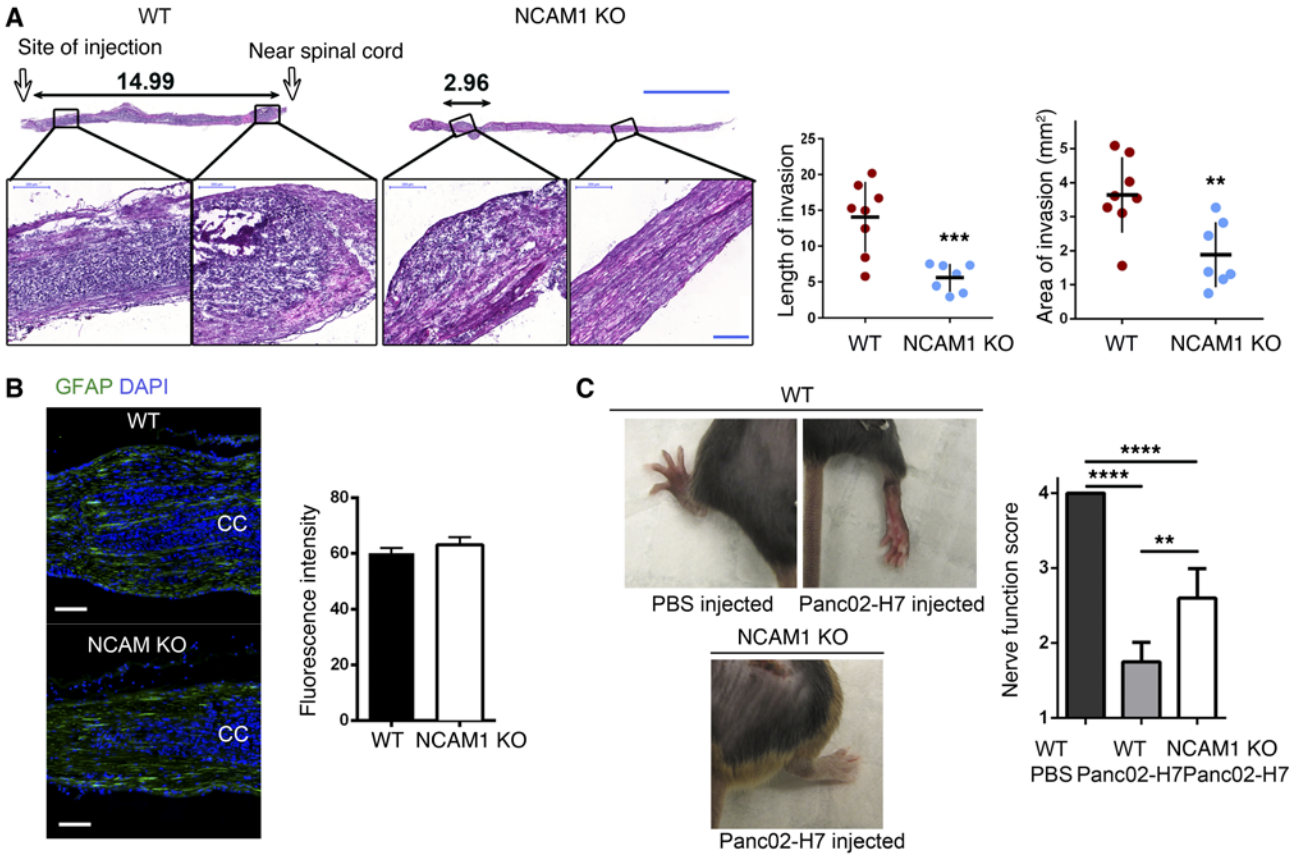

Figure 11. NCAM1 expression by Schwann cells promotes cancer cell invasion in vivo. (**A**) Histological analysis of injected murine sciatic nerves in WT and NCAM1 KO mice showing longer lengths of nerve invasion in WT mice. Representative samples of cancer cell invasion detected by analysis of H&E staining in WT and NCAM1 KO mice. White arrows indicate the site of injection and proximal side of spinal cord. The black arrows indicate the length of invasion with corresponding values (mm). Scale bar: 5 mm (top images) and 0.2 mm (bottom images). Quantification of nerve invasion, as measured by length and area of invasion. Data represent mean ± SD. $^{**}P < 0.005$, $^{***}P < 0.0005$, *t* test, $n = 8$ (NCAM1 WT), $n = 7$ (NCAM1 KO). (**B**) GFAP immunofluorescence staining in WT and NCAM1 KO murine sciatic nerves injected with Panc02-H7 cells was similar. Scale bar: 100 μm. Quantification of the average intensity of GFAP fluorescence did not show a statistically significant difference between WT and NCAM1 KO sections. *t* test, $n = 20$ (WT), $n = 11$ (NCAM1 KO). Data represent mean ± SEM. (**C**) Reduction of perineural invasion in an in vivo assay. Representative images of mouse legs after Panc02-H7 cancer cell injection showing less paralysis in NCAM1 KO mice. In WT mice, injection induced paralysis compared with noninjected leg. Injected NCAM1 KO mice show a reduced paralysis compared with WT mice. Quantification of sciatic nerve function in WT noninjected (WT PBS), WT injected (WT Panc02-H7), and NCAM1 KO injected (NCAM1 KO Panc02-H7) mice. Data represent mean ± SEM. $^{**}P < 0.01$, $^{****}P < 0.0001$, 1-way ANOVA with Holm-Sidak's multiple comparisons test, $n = 10$ per condition.

niscent of the axonal extensions induced and guided by Schwann cells during nerve repair. After nerve injury, Schwann cells dedifferentiate into "repair Schwann cells," while proteins, including GFAP and NCAM1, are upregulated. Here, we showed a similar increase of GFAP$^+$ SCs associated with cancer cells in nerves. Established Schwann cell programs that are normally involved in guiding axons and isolating neurons are inappropriately activated by cancer cells, thereby promoting cancer progression.

Conclusion. These results implicate Schwann cells as important facilitators of cancer invasion and characterize a unique behavior of cells from the microenvironment that promotes cancer cell dispersion. Understanding the ability of Schwann cells to promote cancer invasion has important implications for therapeutic intervention. Therapeutic strategies for nerve repair following spinal cord injury have attempted to harness and enhance the ability of Schwann cells to guide neurons. Interestingly, novel therapeutic strategies to treat perineural invasion may conversely aim to interrupt the guidance function of Schwann cells by preventing Schwann cell–cancer cell contact and targeting NCAM1. The exploitation of normal nerve development and repair processes by cancer cells is a concept that may carry a broader application to other biological systems as well.

Methods

Mouse strains. Nude mice and C57BL/6J mice were obtained from The Jackson Laboratory. NCAM1 KO mice (first described in ref. 36, available from The Jackson Laboratory, strain B6.129P2-Ncam1^{tm1Cgn}) were a generous gift from Urs Rutishauser (Memorial Sloan Kettering Cancer Center).

Primary antibodies and DNA plasmids. The following primary antibodies were used for immunofluorescence staining at the indicated dilutions: mouse anti-Tuj1 antibody (1:100, Millipore, MAB1637), rabbit anti-GFAP antibody (1:1,000, Dako, Z033429-2), mouse anti-S100 antibody (1:250, EMD Millipore, MAB079-1), mouse anti-NCAM1 antibody (used for NCAM1 detection in HEI-286 cells and in human pancreatic specimens, 1:25, Lifespan, LS-B5569-50), rabbit anti-NCAM1 antibody (used for NCAM1 detec-

tion in human pancreatic specimens and in NIH 3T3 cells, 1:100, Millipore, AB5032), rat anti-laminin B2 antibody (Upstate, clone A5 05-206), rabbit anti–myelin protein zero antibody (1:200, abcam, ab31851), rat anti–myelin basic protein antibody (1:200, Millipore, MAB386), mouse anti-keratin antibody (1:50, abcam, ab8068), and rabbit anti-p75 antibody (1:100, Millipore, ab1554). The following primary antibodies were used for Western blot: rabbit anti-NCAM1 antibody (Epitomics, 6740-1) and rabbit anti-GFP antibody (Abcam, ab290). Plasmid pEGFP-F was obtained from Clontech and encodes enhanced GFP fused to the 20–amino acid farnesylation signal from c-Ha-Ras for plasma membrane location. F-RFP, NCAM1-GFP, and NCAM1-Cherry plasmids were previously described (63–65).

Cell lines and cell culture. The human nonneoplastic HEI-286 Schwann cell line was a gift from Filippo Giancotti (Memorial Sloan Kettering Cancer Center) (66). The murine NIH 3T3 and the human pancreatic cancer cell lines Panc1 and MiaPaCa-2 were purchased from ATCC. The murine cell line Panc02-H7 was obtained from Min Li (The University of Texas Health Science Center at Houston, Houston, Texas, USA) (67). Cells were nucleofected or infected with lentivirus for the generation of MiaPaCa-2 F-RFP, Panc1-F-RFP, HEI-286 F-GFP, and NCAM1-depleted HEI-286 cells. MiaPaCa-2 and Panc1 cells were nucleofected using Kit V and program B-024 (Amaxa) and HEI-286 cells were nucleofected using program T-020 (Amaxa). Stable cancer cell lines were generated by selection with G418 (100 μg/ml). Cells with the highest expression level of GFP and RFP were selected by flow cytometry using a BD FACSAria or a Beckman-Coulter MoFlo Cytometer from the Memorial Sloan Kettering Cancer Center facility. Puromycin-resistant MiaPaCa-2 F-RFP and Panc1 F-RFP cells were generated using MISSION pLKO.1-puro empty vector control from Sigma-Aldrich (shc001V) and selection with puromycin (3 μg/ml). To generate NCAM1-depleted HEI-286 cells, we used the following shRNAs (the MISSION pLKO library, Sigma-Aldrich): sh 1 (TRCN0000373085) CCGGCAGCGTTGGAGAGTCCAAATTCTCGAGAATTTGGACTCTCCAACGCTGTTTTTG; sh 2 (TRCN0000373034) CCGGCCGTTCCCTGAAACCGTTAAACTCGAGTTTAACGGTTTCAGGGAACGGTTTTTG; and sh 3: (TRCN0000073460) CCGGCCATGTACCTTGAAGTGCAATCTCGAGATTGCACTTCAAGGTACATGGTTTTTG. MISSION pLKO.1-puro empty vector control transduction particles (shc001V) were used to generate sh control cells. Cells were cultured in 5% CO_2 at 37°C in DMEM (Cellgro) containing 10% fetal bovine serum (Gemini) and 50 U/ml penicillin/streptomycin (Cellgro). Culture media for the sh HEI-286 cells was supplemented with puromycin. Culture media for cells expressing F-GFP and F-RFP were supplemented with G418. Culture media for the puromycin-resistant cancer cells, MiaPaCa-2 F-RFP cells, and Panc1 F-RFP cells were supplemented with both G418 and puromycin. Depletion of NCAM1 in sh HEI-286 cells was verified by Western blotting and immunofluorescence assays using standard protocols. Cell proliferation assays on sh HEI-286 cells were performed using standard counting protocol.

Murine sciatic nerve injection. Sciatic nerve injections were as previously described (21). Briefly, mice (nude athymic mice, NCAM1 KO mice, and C57BL/6J control mice) were anesthetized using isoflurane (1%–3%), and their sciatic nerves were exposed. Sterile PBS and MiaPaCa-2 (150,000 cells) and Panc1 (150,000 cells) human cancer cells and Panc02-H7 (50,000 cells) murine cancer cells were injected into the sciatic nerve under loop magnification using a 10-μl Hamilton syringe. After treatment with bupivacaine for analgesia, the mouse was closed up with surgical sutures. Mice were followed for recovery every day for 72 hours and monitored for nerve function. In the xenograft model, the sciatic nerves of nude mice were injected with human MiaPaCa-2 and Panc1 cancer cells, and signs of nerve invasion appeared at approximately 3 weeks after injection. In the syngeneic model of neural invasion, the sciatic nerves of NCAM1 KO and C57BL/6J control mice were injected with murine Panc02-H7 cells, which can grow in these animals, and signs of invasion appeared at just 3 days after injection.

Murine sciatic nerve function. Sciatic nerve function was measured in WT and NCAM1 KO mice 6 days after injection of Panc02-H7 cells by using the nerve function score. It was graded, from 4 (normal) to 1 (total paw paralysis), according to hind limb paw response to manual extension of the body.

Preparation of murine sciatic nerve and perineural invasion human specimen sections. At indicated times after injection, murine sciatic nerves were dissected up to the spinal cord and embedded in Tissue-Tek OCT (Electron Microscopy Sciences). Sections from human pancreatic specimens were obtained from paraffin blocks that were prepared using a standard protocol. Nonpancreatic human surgical specimens were freshly prepared in normal saline and embedded in O.C.T. The murine and human specimen frozen blocks were serially sectioned longitudinally at 5- and 8-μm thickness, respectively, using a Cryostat microtome (Leica CM1950). Sections were used for H&E and immunofluorescence staining.

Immunofluorescence of human specimen sections and murine sciatic nerve sections. Frozen sections were fixed using 4% paraformaldehyde. All sections were permeabilized and blocked in 3% horse serum, 0.1% Triton X-100/PBS for 1 hour. Primary antibodies diluted in 0.1% horse serum/PBS were incubated overnight at 4°C. Sections were incubated overnight at 4°C with primary antibodies diluted in 0.1% horse serum/PBS. Detection was performed using an appropriate fluorescent secondary antibody (Alexa Fluor 488 [1:500, Invitrogen], Alexa Fluor 568 [1:500, Invitrogen]). Samples were mounted in DAPI containing Vectashield mounting medium. Slides were scanned using Flash Scanner (Perkin Elmer). Morphological assessment and quantification of neural invasion by cancer cells in sciatic nerves were performed using Panoramic Viewer (3D Histech) for the H&E sections. Immunofluorescent sections were analyzed using both Panoramic Viewer (3D Histech) and MetaMorph softwares.

Coculture DRG explants and cancer cells. DRGs were isolated from mice as previously described (21). They were removed, washed in PBS, embedded into 10-μl growth factor–reduced Matrigel matrix (BD Biosciences), and placed on 35-mm glass-bottom dishes (MatTek). DRGs were grown in DMEM containing 10% FBS at 37°C and 5%CO_2. On day 7, fluorescently labeled cancer cells, MiaPaCa-2 and Panc1 (100,000 cells), were added in suspension, and recruitment at neurites was monitored after 2 to 3 days.

Immunofluorescence staining of DRGs. DRGs embedded in Matrigel were fixed in 4% PFA for 1 hour, permeabilized, and blocked in 0.1% Triton, 1% horse serum for 2 hours. Primary antibodies diluted in 0.1% horse serum/PBS were incubated overnight at 4°C, appropriate secondary antibodies (anti-mouse Alexa Fluor 633, anti-rabbit Alexa Fluor 488, 1:500, Invitrogen) were incubated overnight, and the DRG was then immersed in PBS. Images were acquired using inverted Axiovert 200M (Zeiss) microscope and SP5 (Leica) using ×20 0.75-NA water immersion lens.

Radiation treatment of DRGs. DRGs grown in Matrigel for 2 days were treated with X-rays at 12 Gy using a Mark1 generator for removal of dividing cells. The number of Schwann cells was counted in radiated and nonradiated DRGs after 9 days of growth based on morphology during a time-lapse video. Recruitment of cancer cells was measured in radiated or nonradiated DRGs after addition of MiaPaCa-2 or Panc1 cells 3 days later. Imaging for assessment of recruitment at day 9 was performed using an inverted Axiovert 200M Zeiss microscope equipped with EC Plan-Neofluar ×10 0.3-NA Ph1 lens. Since radiated DRGs were found to have decreased growth, quantification was carried out on neurites within a similar size range.

Rescue of radiated DRGs with human Schwann cell line. Isolated murine DRGs were embedded in Matrigel matrix and were treated with X-rays at 12 Gy on day 3 following isolation as described earlier. On day 6 following the radiation treatment, 50,000 cells (HEI-286 F-GFP, HEI-FGFP shC, or HEI-FGFP sh 2 cells or no Schwann cells) were added to radiated DRGs. MiaPaCa-2 F-RFP cells (50,000 cells) were subsequently added to the DRGs on day 7. Images were taken at ×10 magnification with Nikon Eclipse TE 2000-E on days 9 and 10 after radiation, and the recruitment of cancer cells to neurites was quantified as the number of cancer cells directly contacting the neurites.

Live imaging of coculture cancer cells. Dynamic interactions between DRG neurites and MiaPaCa-2 F-RFP cancer cells and between HEI-286 F-GFP cells and MiaPaCa-2 F-RFP cancer cells in 2D and 3D were studied with time-lapse microscopy on an inverted Axiovert 200M (Zeiss) equipped with EC Plan-Neofluar 10X 0.3 NA Ph1 lens, motorized stage, and temperature and CO_2 controlers. Images were recorded every 5 minutes for 24 hours. In 2D culture, MiaPaCa-2 cells were seeded at low density on top of Matrigel and grown as colonies for 7 days; then HEI-286 F-GFP and NCAM1-depleted HEI-286 F-GFP cells were added for 48 hours before time-lapse imaging. In 3D culture, MiaPaCa2 F-RFP and HEI-286 F-GFP cells were coculured in Matrigel for 7 days before imaging. Directionality analyses were performed with ImageJ using the Manual Tracking and Chemotaxis plug-ins. Quantification of directionality is shown as rose diagrams indicating the distribution of migration angles. Quantification of protrusion directionality was performed on cancer cells that were in contact with only one Schwann cell at a time. The images were rotated so that the axis was determined by the position of Schwann cell at the time of initial contact.

Cancer cluster reorganization assay. Cancer cells (MiaPaCa2 F-RFP and Panc1 F-RFP) were grown alone, with Schwann cells (HEI-286 cells or HEI-286 cells expressing NCAM1 sh 2), or with NIH 3T3 cells in a 10-μl drop of Matrigel (50 cells per μl) in a glass bottom Labtek dish. After 7 days of growth, images were acquired using an inverted Zeiss microscope. Image analysis was performed using MetaMorph. The shape of cancer cell clusters was determined using the formula $4\pi A/P^2$ with A standing for the area and P standing for the perimeter of the cancer cell cluster. The shape factor was close to 1 for a rounded shape and close to 0 for an elongated shape.

Invasion assay. HEI-286 F-GFP, HEI-286, or NIH 3T3 cells were seeded in 40 μl Matrigel matrix at 70 cells per μl or as indicated in a 2-chamber insert (Ibidi GmbH) placed in glass-bottom 35-mm MatTek dishes and grown for 6 days in DMEM 10% FBS. Puromycin-resistant red fluorescent cancer cells (MiaPaCa-2 and Panc1 50,000 cells) were then added on top of the Matrigel. In assays involving the removal of Schwann cells, puromycin (3 μg/ml) was added at the time of cancer cell addition. In assays involving the addition of Schwann cell–conditioned medium, Schwann cell–conditioned medium and cancer cells were added simultaneously. Schwann cell–conditioned medium was prepared by centrifuging (1,000 *g* for 10 minutes) medium that was in culture with HEI-286 cells for 3 days. The supernatant was filtered and mixed 1:1 with fresh medium. After 3 days, samples were fixed in 4% paraformaldehyde for 30 minutes for imaging. The coculture was imaged using a Leica SP5 inverted confocal microscope with ×25 0.95-NA and ×10 0.4-NA lenses. The Z-stacks obtained with the ×10 lens were used for quantification of invasion and were 1-mm thick, with a 5-μm step. Images were recorded at 12-bit resolution. Stacks were reconstructed in 3 dimensions using Imaris software (Bitplane), and red fluorescent structures corresponding to cancer cells were quantified using Imaris software. The software determined the number of red cancer cells in an area of interest (size $x = 66$ μm, $y = 296$ μm, $z = 552$ μm) that was about 300 μm below the surface of the Matrigel. The invasion was about 60 cells per area of interest and was considered 100%.

Statistics. Statistical analysis was conducted using unpaired 2-tailed Student's t test, Mann Whitney test, and 1-way ANOVA test with Holm-Sidak test for multiple comparison correction. Statistical significance was defined as $P < 0.05$.

Study approval. The Memorial Sloan Kettering Cancer Center Institutional Review Board approved studies using human tissue samples. Written informed consent was received from the patients. All animal studies were conducted in compliance with Memorial Sloan Kettering Cancer Center institutional guidelines and approved by Memorial Sloan Kettering Cancer Center institutional animal care and use committee.

Author contributions

SD designed and performed experiments, analyzed data, and wrote the manuscript. AL performed experiments and edited the manuscript. YZ, SH, WFM, NC, SYL, FB, CHC, and SH assisted with the animal studies. RLB assisted with the radiation studies. TO and AH provided experimental and conceptual advice and edited the manuscript. TO contributed to live-imaging experiments. EV analyzed pathology slides. RJW designed experiments, wrote the manuscript, and directed the project.

Acknowledgments

We thank Urs Rutishauser for providing the NCAM1 KO mice, Maria Angeles Rabadan for assistance with ImageJ, Ning Fan for assistance with sectioning specimens of perineural invasion, Antoinette Rookard for assistance with maintaining the mice, and Patrick Hilden for assistance with biostatistics. We acknowledge the technical services provided by the Memorial Sloan Kettering Cancer Center molecular cytology and flow cytometry core facilities. This work was supported by NIH grants CA157686 (to R.J. Wong) and P30 CA008748 (Memorial Sloan Kettering Cancer Center support grant). The authors dedicate this work to the memory of Alan Hall.

Address correspondence to: Richard J. Wong, Department of Surgery, Memorial Sloan Kettering Cancer Center, 1275 York Avenue, New York, New York 10065, USA. Phone: 212.639.7638; E-mail: wongr@mskcc.org.

1. Magnon C, et al. Autonomic nerve development contributes to prostate cancer progression. *Science*. 2013;341(6142):1236361.
2. Zhao CM, et al. Denervation suppresses gastric tumorigenesis. *Sci Transl Med*. 2014;6(250):250ra115.
3. Bapat AA, Hostetter G, Hoff Von DD, Han H. Perineural invasion and associated pain in pancreatic cancer. *Nat Rev Cancer*. 2011;11(10):695–707.
4. Liebig C, Ayala G, Wilks JA, Berger DH, Albo D. Perineural invasion in cancer. *Cancer*. 2009;115(15):3379–3391.
5. Condeelis J, Pollard JW. Macrophages: obligate partners for tumor cell migration, invasion, and metastasis. *Cell*. 2006;124(2):263–266.
6. Joyce JA, Pollard JW. Microenvironmental regulation of metastasis. *Nat Rev Cancer*. 2008;9(4):239–252.
7. McAllister SS, Weinberg RA. The tumour-induced systemic environment as a critical regulator of cancer progression and metastasis. *Nat Cell Biol*. 2014;16(8):717–727.
8. Gaggioli C, et al. Fibroblast-led collective invasion of carcinoma cells with differing roles for RhoGTPases in leading and following cells. *Nat Cell Biol*. 2007;9(12):1392–1400.
9. Cheung KJ, Ewald AJ. Illuminating breast cancer invasion: diverse roles for cell-cell interactions. *Curr Opin Cell Biol*. 2014;30:99–111.
10. Jessen KR. Glial cells. *Int J Biochem Cell Biol*. 2004;36(10):1861–1867.
11. Kaplan S, Odaci E, Unal B, Sahin B, Fornaro M. Chapter 2: Development of the peripheral nerve. *Int Rev Neurobiol*. 2009;87:9–26.
12. Fawcett JW, Keynes RJ. Peripheral nerve regeneration. *Annu Rev Neurosci*. 1990;13:43–60.
13. Glenn TD, Talbot WS. Signals regulating myelination in peripheral nerves and the Schwann cell response to injury. *Curr Opin Neurobiol*. 2013;23(6):1041–1048.
14. Kang H, Tian L, Thompson W. Terminal Schwann cells guide the reinnervation of muscle after nerve injury. *J Neurocytol*. 2003;32(5–8):975–985.
15. Scheib J, Höke A. Advances in peripheral nerve regeneration. *Nat Rev Neurol*. 2013;9(12):668–676.
16. Son YJ, Thompson WJ. Nerve sprouting in muscle is induced and guided by processes extended by Schwann cells. *Neuron*. 1995;14(1):133–141.
17. Jessen KR, Mirsky R. The origin and development of glial cells in peripheral nerves. *Nat Rev Neurosci*. 2005;6(9):671–682.
18. Daniloff JK, Levi G, Grumet M, Rieger F, Edelman GM. Altered expression of neuronal cell adhesion molecules induced by nerve injury and repair. *J Cell Biol*. 1986;103(3):929–945.
19. Martini R. Expression and functional roles of neural cell surface molecules and extracellular matrix components during development and regeneration of peripheral nerves. *J Neurocytol*. 1994;23(1):1–28.
20. Neuberger TJ, Cornbrooks CJ. Transient modulation of Schwann cell antigens after peripheral nerve transection and subsequent regeneration. *J Neurocytol*. 1989;18(5):695–710.
21. Gil Z, et al. Paracrine regulation of pancreatic cancer cell invasion by peripheral nerves. *J Natl Cancer Inst*. 2010;102(2):107–118.
22. Demir IE, et al. Investigation of Schwann cells at neoplastic cell sites before the onset of cancer invasion. *J Natl Cancer Inst*. 2014;106(8):dju184.
23. Triolo D, et al. Loss of glial fibrillary acidic protein (GFAP) impairs Schwann cell proliferation and delays nerve regeneration after damage. *J Cell Sci*. 2006;119(pt 19):3981–3993.
24. Ayala GE, et al. In vitro dorsal root ganglia and human prostate cell line interaction: redefining perineural invasion in prostate cancer. *Prostate*. 2001;49(3):213–223.
25. Bakst RL, et al. Radiation impairs perineural invasion by modulating the nerve microenvironment. *PLoS One*. 2012;7(6):e39925.
26. He S, et al. GFRα1 released by nerves enhances cancer cell perineural invasion through GDNF-RET signaling. *Proc Natl Acad Sci U S A*. 2014;111(19):E2008–E2017.
27. Ceyhan GO, et al. Neural invasion in pancreatic cancer: A mutual tropism between neurons and cancer cells. *Biochem Biophys Res Commun*. 2008;374(3):442–447.
28. Chen-Tsai CP, Colome-Grimmer M, Wagner RF. Correlations among neural cell adhesion molecule, nerve growth factor, and its receptors, TrkA, TrkB, TrkC, and p75, in perineural invasion by basal cell and cutaneous squamous cell carcinomas. *Dermatol Surg*. 2004;30(7):1009–1016.
29. Kameda K, et al. Expression of highly polysialylated neural cell adhesion molecule in pancreatic cancer neural invasive lesion. *Cancer Lett*. 1999;137(2):201–207.
30. McLaughlin RB, et al. Nerve cell adhesion molecule expression in squamous cell carcinoma of the head and neck: a predictor of propensity toward perineural spread. *Laryngoscope*. 1999;109(5):821–826.
31. Seki H, Koyama K, Tanaka J, Sato Y, Umezawa A. Neural cell adhesion molecule and perineural invasion in gallbladder cancer. *J Surg Oncol*. 1995;58(2):97–100.
32. Shang J, Sheng L, Wang K, Shui Y, Wei Q. Expression of neural cell adhesion molecule in salivary adenoid cystic carcinoma and its correlation with perineural invasion. *Oncol Rep*. 2007;18(6):1413–1416.
33. Shen FZ, et al. Current research in perineural invasion of cholangiocarcinoma. *J Exp Clin Cancer Res*. 2010;29:24.
34. Vural E, Hutcheson J, Korourian S, Kechelava S, Hanna E. Correlation of neural cell adhesion molecules with perineural spread of squamous cell carcinoma of the head and neck. *Otolaryngol Head Neck Surg*. 2000;122(5):717–720.
35. Campodónico PB, et al. The neural cell adhesion molecule is involved in the metastatic capacity in a murine model of lung cancer. *Mol Carcinog*. 2010;49(4):386–397.
36. Cremer H, et al. Inactivation of the N-CAM gene in mice results in size reduction of the olfactory bulb and deficits in spatial learning. *Nature*. 1994;367(6462):455–459.
37. Liu R, et al. Neural cell adhesion molecule potentiates the growth of murine melanoma via β-catenin signaling by association with fibroblast growth factor receptor and glycogen synthase kinase-3β. *J Biol Chem*. 2011;286(29):26127–26137.
38. Maness PF, Schachner M. Neural recognition molecules of the immunoglobulin superfamily: signaling transducers of axon guidance and neuronal migration. *Nat Neurosci*. 2007;10(1):19–26.
39. Neugebauer KM, Tomaselli KJ, Lilien J, Reichardt LF. N-cadherin, NCAM, and integrins promote retinal neurite outgrowth on astrocytes in vitro. *J Cell Biol*. 1988;107(3):1177–1187.
40. Saffell JL, Ashton SV, Walsh FS, Doherty P. The changing role of NCAM as a neurite outgrowth-promoting molecule during development. *Biochem Soc Trans*. 1992;20(2):410–412.
41. Zecchini S, et al. The adhesion molecule NCAM promotes ovarian cancer progression via FGFR signalling. *EMBO Mol Med*. 2011;3(8):480–494.
42. Cavel O, et al. Endoneurial macrophages induce perineural invasion of pancreatic cancer cells by secretion of GDNF and activation of RET tyrosine kinase receptor. *Cancer Res*. 2012;72(22):5733–5743.
43. Marchesi F, et al. The chemokine receptor CX3CR1 is involved in the neural tropism and malignant behavior of pancreatic ductal adenocarcinoma. *Cancer Res*. 2008;68(21):9060–9069.
44. Lv CY, et al. Preliminary study correlating CX3CL1/CX3CR1 expression with gastric carcinoma and gastric carcinoma perineural invasion. *World J Gastroenterol*. 2014;20(15):4428–4432.
45. Doumas S, et al. Fractalkine (CX3CL1) and fractalkine receptor (CX3CR1) in squamous cell carcinoma of the tongue: markers of nerve invasion? *Oral Maxillofac Surg*. 2015;19(1):61–64.
46. Roh-Johnson M, et al. Macrophage contact induces RhoA GTPase signaling to trigger tumor cell intravasation. *Oncogene*. 2013;33(33):4203–4212.
47. Tamura D, Hiraga T, Myoui A, Yoshikawa H, Yoneda T. Cadherin-11-mediated interactions with bone marrow stromal/osteoblastic cells support selective colonization of breast cancer cells in bone. *Int J Oncol*. 2008;33(1):17–24.
48. Li R, Wheeler T, Dai H, Ayala G. Neural cell adhesion molecule is upregulated in nerves with prostate cancer invasion. *Hum Pathol*. 2003;34(5):457–461.
49. Kolkova K, Novitskaya V, Pedersen N, Berezin V, Bock E. Neural cell adhesion molecule-stimulated neurite outgrowth depends on activation of protein kinase C and the Ras-mitogen-activated protein kinase pathway. *J Neurosci*. 2000;20(6):2238–2246.
50. McCubrey JA, et al. Roles of the Raf/MEK/ERK pathway in cell growth, malignant transformation and drug resistance. *Biochim Biophys Acta*. 2007;1773(8):1263–1284.
51. Roberts PJ, Der CJ. Targeting the Raf-MEK-ERK mitogen-activated protein kinase cascade for the treatment of cancer. *Oncogene*. 2007;26(22):3291–3310.
52. Urtreger AJ, Kazanietz MG, Bal de Kier Joffé ED. Contribution of individual PKC isoforms to breast cancer progression. *IUBMB Life*. 2012;64(1):18–26.
53. Wells A, Grandis JR. Phospholipase C-gamma1 in tumor progression. *Clin Exp Metastasis*. 2003;20(4):285–290.
54. Lehembre F, et al. NCAM-induced focal adhesion assembly: a functional switch upon loss of E-cadherin. *EMBO J*. 2008;27(19):2603–2615.

55. Schreiber SC, et al. Polysialylated NCAM represses E-cadherin-mediated cell-cell adhesion in pancreatic tumor cells. *Gastroenterology*. 2008;134(5):1555–1566.
56. Shi Y, et al. Neural cell adhesion molecule modulates mesenchymal stromal cell migration via activation of MAPK/ERK signaling. *Exp Cell Res*. 2012;318(17):2257–2267.
57. Esni F, et al. Neural cell adhesion molecule (N-CAM) is required for cell type segregation and normal ultrastructure in pancreatic islets. *J Cell Biol*. 1999;144(2):325–337.
58. Kolkova K, Stensman H, Berezin V, Bock E, Larsson C. Distinct roles of PKC isoforms in NCAM-mediated neurite outgrowth. *J Neurochem*. 2005;92(4):886–894.
59. Ushiki T, Ide C. Autonomic nerve networks in the rat exocrine pancreas as revealed by scanning and transmission electron microscopy. *Arch Histol Cytol*. 1988;51(1):71–81.
60. Sunami E, et al. Morphological characteristics of Schwann cells in the islets of Langerhans of the murine pancreas. *Arch Histol Cytol*. 2001;64(2):191–201.
61. Cravioto H. The role of Schwann cells in the development of human peripheral nerves. An electron microscopic study. *J Ultrastruct Res*. 1965;12(5):634–651.
62. Son YJ, Thompson WJ. Schwann cell processes guide regeneration of peripheral axons. *Neuron*. 1995;14(1):125–132.
63. Cau J, Hall A. Cdc42 controls the polarity of the actin and microtubule cytoskeletons through two distinct signal transduction pathways. *J Cell Sci*. 2005;118(pt 12):2579–2587.
64. Müsch A, Cohen D, Kreitzer G, Rodriguez-Boulan E. cdc42 regulates the exit of apical and basolateral proteins from the trans-Golgi network. *EMBO J*. 2001;20(9):2171–2179.
65. Deborde S, et al. Clathrin is a key regulator of basolateral polarity. *Nature*. 2008;452(7188):719–723.
66. Li W, et al. Merlin/NF2 suppresses tumorigenesis by inhibiting the E3 ubiquitin ligase CRL4(DCAF1) in the nucleus. *Cell*. 2010;140(4):477–490.
67. Wang Y, et al. Genomic sequencing of key genes in mouse pancreatic cancer cells. *Curr Mol Med*. 2012;12(3):331–341.